Smooth light curves from a bumpy ride: relativistic blast wave encounters a density jump

Ehud Nakar[1]★ and Jonathan Granot[2]★

[1]*Theoretical Astrophysics, Caltech, Pasadena, CA 91125, USA*
[2]*KIPAC, Stanford University, PO Box 20450, MS 29, Stanford, CA 94309, USA*

ABSTRACT

In the standard forward shock model for gamma-ray burst (GRB) afterglow, the observed afterglow emission is synchrotron radiation from a quasi-spherical, adiabatic, self-similar, relativistic blast wave, that propagates into the external medium. This model predicts a smooth light curve where the flux scales as a power law in time, and may at most smoothly transition to a different power law. However, some GRB afterglow light curves show significant variability, which often includes episodes of rebrightening. Such temporal variability had been attributed in several cases to a large enhancement in the external density, or a density 'bump', that is encountered by the self-similar adiabatic blast wave. Here we examine the effect of a sharp increase in the external density on the afterglow light curve in this scenario by considering, for the first time, a full treatment of both the hydrodynamic evolution and the radiation. To this end we develop a semi-analytic model for the light curve and carry out numerical simulations using a one-dimensional hydrodynamic code together with a synchrotron radiation code. Two spherically symmetric cases are explored in detail – a density jump in a uniform external medium (which is used to constrain the effect of a density clump) and a wind termination shock. We find that even a very sharp (modelled as a step function) and large (by a factor of $a \gg 1$) increase in the external density does not produce sharp features in the light curve, and cannot account for significant temporal variability in GRB afterglows in the forward shock model. For a wind termination shock, the light curve smoothly transitions between the asymptotic power laws over about one decade in time, and there is no rebrightening in the optical or X-rays that could serve as a clear observational signature. For a sharp jump in a uniform density profile, we find that the maximal deviation $\Delta\alpha_{max}$ of the temporal decay index α from its asymptotic value (at early and late times) is bounded (e.g, $\Delta\alpha_{max} < 0.4$ for $a = 10$); $\Delta\alpha_{max}$ slowly increases with a, converging to $\Delta\alpha_{max} \approx 1$ at very large a values. Therefore, no optical rebrightening is expected in this case as well. In the X-rays, while the asymptotic flux is unaffected by the density jump, the fluctuations in α are found to be comparable to those in the optical. Finally, we discuss the implications of our results for the origin of the observed fluctuations in several GRB afterglows.

Key words: hydrodynamics – shock waves – gamma-rays: bursts.

1 INTRODUCTION

Gamma-ray bursts (GRBs) are produced by a relativistic outflow from a compact source. The outflow sweeps up the external medium and drives a strong relativistic shock into it. Eventually, the outflow is decelerated (by $p\mathrm{d}V$ work across the contact discontinuity that separates the ejecta and the shocked external medium) and most of

the kinetic energy is transferred to the shocked external medium (for recent reviews see Piran 2005; Meszaros 2006; Nakar 2007). According to this external shock model, the shocked gas assumes a self-similar profile of a quasi-spherical, adiabatic, relativistic blast wave (Blandford & McKee 1976) within 10^2–10^4s after the burst. This shocked gas is the source of the long-lived, slowly decaying (with a roughly constant radiated energy per decade in time), afterglow emission that is detected in the X-rays, optical, and radio for days, weeks, and months, respectively, after the GRB. The afterglow emission is thought to be predominantly synchrotron radiation. This

★E-mail: udini@tapir.caltech.edu (EN); granot@slac.stanford.edu (JG)

is supported both by the broad-band spectrum and by the detection of linear polarization at the level of a few per cent in the optical [or near-infrared (NIR)] afterglow of several GRBs (see Covino et al. 2003, and references therein). Inverse-Compton scattering of the synchrotron photons might dominate the observed flux in the X-rays in some cases (Wei & Lu 1998; Panaitescu & Kumar 2000; Harrison et al. 2001; Sari & Esin 2001).

In the pre-*Swift* era, the best monitoring of GRB afterglow light curves was, by far, in the optical. Most afterglow light curves showed a smooth power-law decay (Stanek et al. 1999; Laursen & Stanek 2003; Gorosabel et al. 2006), and often also a smooth achromatic transition to a steeper power-law decay that is attributed to the outflow being collimated into a narrow jet (Rhoads 1999; Sari, Piran & Halpern 1999). It has been argued (Wang & Loeb 2000) that the smoothness of the afterglow light curve is directly related to (and thus enables to constrain) the smoothness of the external density field. Nevertheless, some optical afterglows have shown significant temporal variability, with strong deviations from the more typical smooth power-law behaviour. The best examples are GRBs 021004 (Pandey et al. 2002; Bersier et al. 2003; Fox et al. 2003) and 030329 (Matheson et al. 2003; Sato et al. 2003; Lipkin et al. 2004; Uemura et al. 2004).

Possible explanations for such temporal variability in GRB afterglow light curves within the external shock framework include variations in the external density (e.g. Wang & Loeb 2000; Dai & Lu 2002; Lazzati et al. 2002; Dai & Wu 2003; Nakar, Piran & Granot 2003; Nakar & Piran 2003; Ioka, Kobayashi & Zhang 2005; Pe' er & Wijers 2006; Zhang et al. 2006), or in the energy of the afterglow shock. The latter includes energy injection by 'refreshed shocks' – slower shells of ejecta that catch up with the afterglow shock on long time-scales (e.g. Rees & Mészáros 1998; Kumar & Piran 2000a; Sari & Mészáros 2000; Ramirez-Ruiz, Merloni & Rees 2001a; Björnsson et al. 2002; Granot, Nakar & Piran 2003; Ioka, Kobayashi & Zhang 2005; Panaitescu 2005) or a 'patchy shell' – angular inhomogeneities within the outflow (e.g. Kumar & Piran 2000b; Heyl & Perna 2003; Nakar et al. 2003; Nakar & Oren 2004; Ioka et al. 2005). Another possible cause for variability in the afterglow light curve, although it is expected to be quite rare, is microlensing by an intervening star in a galaxy that happens to be close to our line of sight. GRB 000301C exhibited an achromatic bump in its optical to NIR light curves that peaked after ∼4 d (Berger et al. 2000; Masetti et al. 2000; Sagar et al. 2000) which had been interpreted as such a microlensing event (Garnavich, Loeb & Stanek 2000; Gaudi, Granot & Loeb 2001; Baltz & Hui 2005), although other interpretations such as a bump in the external density have also been suggested (Berger et al. 2000).

Recent observations by *Swift* have found flares in the early X-ray afterglows of many GRBs (Burrows et al. 2005; Falcone et al. 2006; Nousek et al. 2006; O' brien et al. 2006) which are probably due to late-time activity of the central source (Nousek et al. 2006; Zhang et al. 2006; Krimm et al. 2007). Early optical variability also appears to be more common than previously thought (e.g. Stanek et al. 2007), although it is not yet clear if it is caused by similar mechanisms as the late-time optical variability that had been detected before *Swift*.

The most natural forms of variations in the external density are either clumps on top of a smooth background density distribution, or a global abrupt change in density with radius. The latter can be, for example, the termination shock of the wind from the massive star progenitor of a long-soft GRB (Wijers 2001). Such a stellar wind environment may have a richer structure and can include an abrupt increase in density with radius at the contact discontinuity between shocked wind from two different evolutionary stages of the progenitor star, as well as clumps that are formed due to Rayleigh–Taylor instability (Ramirez-Ruiz et al. 2005; Eldridge et al. 2006).[1] Density clumps with a mild density contrast may also be formed due to turbulence in the external medium. Furthermore, the external density profile is expected to vary between different progenitor models (Fryer, Rockefeller & Young 2006). The recurring variability that had been observed in several optical afterglows was attributed to such density clumps in the external medium (e.g. Lazzati et al. 2002; Nakar et al. 2003). The expected observational signatures of the afterglow shock running into the wind termination shock of the massive star progenitor have also been considered (Ramirez-Ruiz et al. 2001b, 2005; Wijers 2001; Eldridge et al. 2006; Pe' er & Wijers 2006). These works suggest that a wind termination shock will have a clear observational signature in the form of a rebrightening in the optical afterglow light curve, before approaching the new shallower decay slope corresponding to the uniform density of the shocked wind.

All models for the observed light curve from an adiabatic relativistic blast wave that propagates into a variable external density use various approximations. These include mainly approximations for the hydrodynamics, photon arrival times to the observer, and microphysics of the emitting region. The most common approximations for the hydrodynamics neglect the back-reaction of density enhancement on the already shocked fluid, that is, the reverse shock. Another common approximation is to neglect the difference in the arrival time to the observer of photons emitted at the same radius from different angles with respect to the line of sight, that is, the angular smoothing. The microphysics of the emitting region is approximated in all treatments by an ad hoc standard parametrization of the magnetic field and the relativistic electrons distribution.

The first to model an adiabatic external shock with fluctuating circumburst density were Wang & Loeb (2000), who considered the statistical properties of the fluctuating light curve when the external density fluctuations are a small perturbation over a constant density. Dai & Lu (2002) considered the line-of-sight emission from an arbitrarily large density jump by calculating the reverse shock that is generated by the encounter of the blast wave with this jump. Lazzati et al. (2002) and Nakar & Piran (2003) took into account the angular smoothing effect (with different levels of approximations) but ignored the reverse shock. Later treatments, as well as calculations of the signature of a wind termination shock, all approximate these two effects to some degree.

Here we revisit the affects of an external density jump on the afterglow light curve in the adiabatic external shock model, with a full treatment of both the hydrodynamics and the photon arrival times, for a spherically symmetric configuration. We solve in detail the case of a relativistic, adiabatic, self-similar blast wave that propagates into a spherically symmetric external density with a single density jump (by a factor of $a > 1$) at some radius R_0, while the density at smaller and larger radii is a (generally different) power law in radius. This is done by constructing a semi-analytic model for the observed flux due to synchrotron emission at different power-law segments (PLSs) of the spectrum and by carrying out numerical simulations. The semi-analytic model is based on a combination of the solutions presented by Dai & Lu (2002) and Nakar & Piran (2003) and it takes into account the effect of the reverse shock on

---

[1] Ramirez-Ruiz et al. (2005) find that the clump formation may also involve the Vishniac instability, and once such clumps are formed they stand a reasonable chance to survive until the time of the core collapse of the progenitor star.

the hydrodynamics and on the emissivity, as well as the effect of the spherical geometry on the arrival time of photons to the observer.

Being semi-analytic, however, this model uses some approximations for the hydrodynamic evolution and the resulting radiation. Therefore, we also perform numerical simulations in which the light curves are calculated using a hydrodynamic+radiation numerical code. This code self-consistently calculates the radiation and evolves the electron distribution in every fluid element, which corresponds to a computational cell of the one-dimensional Lagrangian hydrodynamic code. The results of this code are used to obtain light curves in cases of special interest and near spectral break frequencies, as well as to verify the quality of the semi-analytic model, which is found to be in good agreement with the numerical results. These calculations are much more accurate than those presented in previous works, and our results are different. In all cases, we find a very smooth transition to the new asymptotic power law, with no rebrightening for an initially decaying light curve.

Our case study of a wind termination shock provides a good, realistic representation of the expected physical configuration, which features a single roughly spherical density jump. Thus, our results provide the accurate observational signature of a wind termination shock at a radius of $\sim 10^{17}$–10^{18} cm, where for typical wind and GRB parameters the external shock is expected to be adiabatic, self-similar and relativistic. If the circumburst medium has a constant density [as expected for an interstellar medium (ISM)], then the cases that we solve are not directly applicable, as no spherically symmetric density jump is expected in such a medium. However, as we discuss below (Section 2), our solution can be used in order to put upper limits on the rebrightening expected during the encounter of the blast wave with a dense clump.

In Section 2, we discuss the assumptions, limitations, and applicability of our solution. Next, in Section 3, we develop the semi-analytic model. First, in Section 3.1 a simple analytic model is constructed for the hydrodynamics, which agrees very well with our numerical results. In Section 3.2, we then construct a semi-analytic model for the observed flux density. Specific case studies (Section 4) are then analysed in detail, for a wind termination shock (Section 4.1) and for a spherical density jump in a uniform medium (Section 4.2). The light curves for these cases are also calculated using the numerical code (described in Appendix A). The effect of proximity to a break frequency around the time of the density jump is investigated in Section 4.3, and our main conclusions are found to remain valid also in the vicinity of the break frequencies. The next section (Section 5) is devoted to a discussion of the expected observational signatures of density clumps on top of a smooth underlying external density distribution. Such density clumps are found to have a very weak observational signature which would be very hard to detect. In Section 6, we discuss the implications of our results for the origin of the observed fluctuations in several GRB afterglows. Our conclusions are discussed in Section 7.

2 ASSUMPTIONS, LIMITATIONS, AND APPLICABILITY

In this work, we solve in detail an ideal case of a spherical, relativistic, self-similar, adiabatic blast wave that encounters a single spherically symmetric density jump. Thus, before presenting the solution, we discuss here in some detail the different assumptions that are made when deriving the solution and the conditions under which it is applicable to GRB afterglows. Throughout our discussion, we assume the standard microphysical parametrization in which the fraction of the total internal energy in the magnetic field is a con-

stant in space and time, while the fraction of the internal energy in electrons is constant in time just behind the shock, but generally decreases with time in each shocked fluid element (and therefore with the distance behind the shock at a fixed time) due to radiative and adiabatic losses.

(i) *Relativistic.* Our solution assumes that the blast wave is relativistic both before and after the density jump. Thus it is applicable only before the Newtonian transition time, T_{NR}, as calculated assuming no density jump, which typically ranges from several months to several years after the burst for both an ISM and a wind (e.g. Wijers, Rees & Meszaros 1997; Chevalier & Li 2000). If the density jump is large then in order for the blast wave to remain relativistic also after the jump it should take place at an even earlier time (smaller radius). For a large density contrast, $a \gg 1$, in a constant external density (ISM) our solution is applicable at $T \ll a^{-2/3} T_{NR}$, where T_{NR} is evaluated for the density before the jump. For a wind termination shock ($a = 4$) the blast wave remains relativistic also after the density jump if the termination shock is at $R_0 \lesssim 1(E_{53}/A_*)$ pc, corresponding to an observer time of $T_0 \sim 100(1 + z)(E_{53}/A_*)$ d, where z is the GRB redshift, $E = E_{53} 10^{53}$ erg is the isotropic equivalent energy of the blast wave, and $A_* = (\dot{M}/4\pi v_w)/(5 \times 10^{11} \, \text{g cm}^{-1}) = \dot{M}_{-5}/v_{w,8}$ where $\dot{M} = 10^{-5} \dot{M}_{-5} \, \text{M}_\odot \, \text{yr}^{-1}$ and $v_w = 10^8 v_{w,8} \, \text{cm s}^{-1}$ are the wind mass-loss rate and velocity, respectively.

In fact, we expect very different results in the Newtonian regime, where an external density jump can cause a large amplitude sharp increase in the observed flux. This is fully consistent with our results, since the two main causes of the smooth light curves we obtain in the relativistic regime become insignificant in the Newtonian regime. The first is the angular smoothing due to different photon arrival times from the same radius at different angles from our line of sight. Obviously, light-travel effects become unimportant deep in the Newtonian regime. This enables very sharp features in the light curve in the Newtonian case, which are not possible in the Relativistic case due to angular smoothing. The second effect is the difference between the emissivity in the comoving frame of the emitting fluid (which increases due to the density jump) and in the laboratory frame (which actually slightly decreases, due to the drop in the Lorentz factor). Again, this effect becomes unimportant in the Newtonian regime, where the emissivity in both frames is almost identical, and they both increase due to a density jump, causing a rebrightening in the observed light curve.

(ii) *Self-similarity.* The forward shock is expected to become self-similar after the original relativistic outflow is decelerated significantly and most of its energy is transferred to the shocked external medium. For typical parameters of an ISM or a wind, the self-similar phase is expected to start on a time-scale that is comparable to the burst duration for long GRBs, namely $T_{dec} \sim T_{GRB} \sim 10$–$10^3$ s after the start of the burst (e.g. Sari & Piran 1995; Chevalier & Li 2000). An additional requirement is that the density at $R < R_0$ behaves as a power law with radius. This implies that the rebrightening limits that we present here are (strictly) applicable only to the case when a rebrightening is observed following a smooth power-law decay. The self-similarity assumption implies that the derived limits do not apply for models that invoke circumburst density fluctuations in order to produce light curve variability at very early times ($T < T_{dec}$), before the outflow decelerates and transfers most of its energy to the circumburst medium. For example, Dermer & Mitman (1999) and Dermer (2007b) analyse the interaction of a thin shell before it decelerates with density clumps , thereby allowing the shell to remain thin and having a negligible emission from regions of the shell that do not interact with the density clumps. They show that

in this scenario clumps with opening angles much smaller than the inverse of the shell Lorentz factor can produce highly variable light curve.

(iii) *Adiabaticity.* Our solution considers an adiabatic blast wave. Significant energy losses, which could alter the hydrodynamics, may take place if the electrons are in the fast-cooling regime (i.e. radiate most of their energy on a time-scale much sorter than the dynamical time), if the initial fraction of the internal energy in the radiating electrons, ϵ_e, is high. An alternative energy-loss channel is the depletion of the energy in an accelerated hadronic component, if the external shock is a highly efficient cosmic-ray accelerator (Dermer 2007a). For typical parameters the blast wave becomes adiabatic within 10^2–10^3s after the burst, but in bursts with very high magnetic field behind the external shock and/or large isotropic energy and high external density the blast wave may be radiative for much longer. Fortunately, a radiative blast wave has an observational signature which is a fast decay at high frequencies, for example, X-rays, where the emitted energy per decade in time is roughly proportional to the blast wave energy. Such fast decay is observed in some afterglows up to $\sim 10^2$–10^3 s after the burst, and as suggested by Dermer (2007a), may be a result of a radiative phase. Therefore, our solution is not applicable to the early rapid decay phase (when such phase is observed), but only to later stages where the X-ray flux decay indicates that the blast wave is adiabatic. In a large fraction of *Swift* GRBs the X-ray flux decay indicates an adiabatic blast wave starting as soon as the prompt gamma-ray emission ends (e.g. Panaitescu 2007).

(iv) *Sphericity.* The hydrodynamic solution that we use assumes that the blast wave is spherical. This assumption breaks down for a jet, after its Lorentz factor γ drops below the inverse of this half-opening angle, which corresponds to times after an achromatic jet break appears in the afterglow light curve (Rhoads 1997), $T > T_{\text{jet}}$. Thus rebrightening limits that we present here are applicable to the pre-jet-break phase ($T < T_{\text{jet}}$). Rough estimates of the rebrightening limits in the post-jet-break phase can be obtained by considering the hydrodynamics as a wedge taken out of a spherical solution (a slowly spreading jet is supported by numerical simulations; Granot et al. 2001; Cannizzo, Gehrels & Vishniac 2004). The variability time-scales observed in this scenario are shorter than those expected if the jet spreads sideways so that its half-opening angle remains roughly $1/\gamma$, and any variability is smoothed by the large angular time-scale (see further discussion of limits on post-jet-break rebrightening in the context of GRB 030329, in Section 6). Being spherical, our solution does not constrain models in which the blast wave does not propagate, at least approximately, radially, such as the cylindrical jet model (e.g. Huang et al. 2002; Tam et al. 2005).

(v) *Density clumps.* Another way in which the spherical symmetry may be broken is due to a-spherical density clumps, which may occur in a clumpy ISM. A full solution of the light curve that is produced by density clumps requires a study of the blast wave exit from the clump, that is the case of a drop in the density. Furthermore, clumps that are small enough so the emission from their sides (in the tangential direction) can be observed, cannot be accurately calculated using one-dimensional hydrodynamics. Finally, if many clumps with large density contrast are present, then there is no point where the blast wave is self-similar and thus a full separate solution (most likely numerical) is required for each individual clump, taking into account the global specific clump configuration. While detailed solutions of density drops as well as two- or three-dimensional relativistic hydrodynamic problems are beyond the scope of this paper, our results can still be used to put an upper limit to the case of a

self-similar blast wave that hits a dense clump or many clumps at the same radius. The reason for this is that both a density drop and observing the edges of a small clump lead to a drop in the luminosity compared to the case that we study here. Therefore, the rebrightening of the light curves that we present here is an *upper limit* to the actual rebrightening in the case that a blast wave in a constant density medium hits a dense clump.

To conclude, the light curves that we present here are an accurate description of the observational signature expected, within the external shock model, from a wind termination shock that is located in the range $R_0 \sim 0.01$–1 pc and is observed $\sim 10^3$–10^6 s after the burst. The light curves that we obtain for a constant density medium constrain the rebrightening expected from a density clump in case that before the rebrightening the optical and X-ray light curves decay roughly as a power law with index $-\alpha \approx 0.5$–1.5 where $\alpha \equiv$ d $\log F_\nu$/d $\log T$ (i.e. $t^{-0.5} - t^{-1.5}$).

3 SEMI-ANALYTIC MODEL FOR A SPHERICAL JUMP IN THE EXTERNAL DENSITY

In this section, we model a spherical relativistic blast wave that propagates into a power-law external density profile ($\rho_{\text{ext}} = Ar^{-k}$ with $k < 3$) which has a single sharp density jump (by a factor $a > 1$) at some radius $r = R_0$. The power-law index, k, of the external density is allowed to be different at $r < R_0$ (k_0) and at $r > R_0$ (k_1).

The hydrodynamic evolution, as well as the resulting contribution to the light curves, can be roughly separated into three phases corresponding to the following ranges of the radius R of the forward shock: (i) at $R < R_0$ the blast wave follows a self-similar evolution (Blandford & McKee 1976, hereafter BM), (ii) at $R = R_0$ a reverse shock forms which crosses most of the shell of previously shocked material (that had been swept up at $r < R_0$) at $R = R_1$, while the forward shock continues ahead of the density jump but with a reduced Lorentz factor, and (iii) at $R > R_1$ the forward shock relaxes into a new self-similar evolution corresponding to the new density profile at $r > R_0$. In the following, we first approximate the hydrodynamic evolution of the different shocks during these three phases and then calculate the resulting light curves.

3.1 Hydrodynamics

Consider a spherical ultra-relativistic blast wave (identified with the afterglow shock), which is well described by the self-similar BM solution at $R < R_0$, that propagates into the following external density profile:

$$\rho_{\text{ext}} = \begin{cases} A_0 r^{-k_0} & r < R_0 \,, \\ A_1 r^{-k_1} & r > R_0. \end{cases} \tag{1}$$

The amplitude of the density jump, that is, the factor by which the density increases at $r = R_0$, is given by

$$a \equiv \lim_{\epsilon \to 0} \frac{\rho_{\text{ext}}[(1+\epsilon)R_0]}{\rho_{\text{ext}}[(1-\epsilon)R_0]} = \frac{A_1}{A_0} R_0^{k_0-k_1}, \tag{2}$$

and is assumed to be larger than unity. The afterglow shock encounters the jump in the external density profile at a laboratory frame time $t_0 = [1 + 1/2(4 - k_0)\Gamma_4^2]R_0/c \approx R_0/c$, where c is the speed of light, Γ_4 is the Lorentz factor of the shock front just before it encounters the density bump at $r = R_0$, and the corresponding Lorentz factor of the fluid just behind the shock is denoted by $\gamma_4 = \Gamma_4/\sqrt{2}$. At $t < t_0$ there are three regions: the region behind

the afterglow shock (subscript '4') is described by the BM solution with $(A, k) = (A_0, k_0)$, and the two regions of cold unperturbed external medium (subscripts '0' and '1' at $r < R_0$ and $r > R_0$, respectively).

When the afterglow shock encounters the jump in the external density, a reverse shock is driven into the hot BM shell, while a forward shock propagates into the cold higher density external medium at $r > R_0$. At this stage region '0' no longer exists, but two new regions are formed so that altogether there are four regions: (i) the cold unperturbed external medium ahead of the forward shock with a density $\rho_{\text{ext}} = A_1 r^{-k_1}$, (ii) the shocked external medium originating from $r > R_0$, (iii) the portion of the BM shell that has been shocked by the reverse shock (corresponding to doubly shocked external medium originating at $r < R_0$), and (iv) the unperturbed portion of the BM solution which has not yet been shocked by the reverse shock (i.e. singly shocked external medium originating from $r < R_0$). These regions are denoted by subscripts '1', '2', '3' and '4', respectively. Regions 2 and 3 are separated by a contact discontinuity.

Immediately after t_0 [or more precisely, at $0 < (t - t_0)/t_0 \ll a^{-1/2}$] the reverse shock reaches only a very small part of the BM profile (just behind the contact discontinuity) which corresponds to values $\chi - 1 \ll 1$ of the self-similar variable, χ defined in BM, so that at this early stage the conditions in this region may be approximated as being constant with the values just behind the shock for the BM profile with $(A, k) = (A_0, k_0)$ at $t = t_0$ (i.e. when the shock radius is $R = R_0$). Since we are interested in a small range in radius, $\Delta R \ll R_0$, we can use a planar geometry and solve the relevant Riemann problem. Region 4 is described by the BM solution while in region 1 we have $\rho_1 = w_1/c^2 = n_1 m_p = A_1 r^{-k_1}$, $p_1 = e_1 = 0$ and $\gamma_1 = 1$, where m_p is the proton mass. The pressure p, internal energy density e, enthalpy density w, rest mass density ρ, and number density n are measured in the proper frame (i.e. the fluid rest frame). We consider a relativistic afterglow shock, $\gamma_4 \gg 1$, and a density contrast which is not too large such that even after the afterglow shock crosses the density bump it will still be relativistic (i.e. $\gamma_4 \gg \psi \sim a^{1/4}$, see equation 3). Under these conditions, in regions 2 and 3 the fluid is relativistically hot, $\rho_2 c^2 \ll p_2$ and $\rho_3 c^2 \ll p_3$. Therefore, the adiabatic index in regions 2, 3 and 4 is 4/3, implying $p_i = e_i/3 = w_i/4$ in these regions. This leaves eight unknown quantities: γ, n and e in regions 2 and 3, as well as the Lorentz factors of the reverse shock, Γ_r, and of the forward shock, Γ_f. Correspondingly, there are eight constraints: three from the shock jump conditions at each of the two shocks, and two at the contact discontinuity: $e_2 = e_3$ and $\gamma_2 = \gamma_3$. The shock jump conditions simply state the conservation of energy, momentum, and particle number across the shock, which is equivalent to the continuity of their corresponding fluxes. At the rest frame of the shock front they correspond to the continuity of $w\gamma^2 v$, $w\gamma^2(v/c)^2 + p$ and $n\gamma v$, respectively, across the shock (where v is the fluid velocity measured in that frame, while p, n, and w are measured in the rest frame of the fluid). Unless stated otherwise, all velocities and Lorentz factors are measured in the rest frame of the unperturbed external medium, which is identified with the laboratory frame where the flow is spherical.

Under the above assumptions and for $\gamma_2 = \gamma_3 \gg 1$, we obtain

$$\left(\frac{\gamma_4}{\gamma_3}\right)^2 \equiv \psi^2 = \frac{3a - 4}{\sqrt{(12/a)}(a - 1) - 1}. \tag{3}$$

In the limit of a relativistic reverse shock ($a \gg 1$) equation (3) reduces to $\psi = \gamma_4/\gamma_3 \approx (3a/4)^{1/4}$.
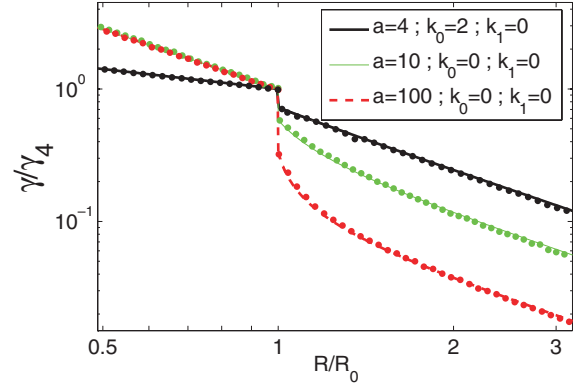

Figure 1. The Lorentz factor of the forward shock as a function of radius for three different density profiles that are described by equation (1) (see the legend for the parameters of each profile). The solid lines show our analytic approximation (equation 6) while the dots are the results of a hydrodynamic simulation.

The Lorentz factor, γ, of the fluid behind the forward shock as a function of[2] $\tilde{R} \equiv R/R_0$ is $\gamma(\tilde{R} < 1) = \gamma_4 \tilde{R}^{(3-k_0)/2}$ before the density jump and $\gamma = \psi^{-1} \gamma_4$ immediately after the density jump. A simple and useful analytic model for $\gamma(\tilde{R} > 1)$ is obtained using the energy conservation equation while replacing the mass collected up to R_0, $M_0 = 4\pi A_0 R_0^{3-k_0}/(3 - k_0)$, by an effective mass $M_{\text{eff},0} = \psi^2 M_0$. The reasoning behind the factor of ψ^2 is to account for the fact that just after the density jump the bulk Lorentz factor and the average particle random Lorentz factor in region 4 (γ_4) is a factor of ψ higher than that in region 2 ($\gamma_2 = \gamma_3$), so that the energy in region 4 is $\approx M_0 \gamma_4^2 = \psi^2 M_0 \gamma^2$. As a result the expression for energy conservation at $R > R_0$ is approximated by

$$E = \left[C_0 \psi^2 M_0 + C_1 M_1(R) \right] \gamma^2(R) c^2 = \text{constant}, \tag{4}$$

where $C_i = 4(3 - k_i)/(17 - 4k_i)$ (this is valid for $k_i < 3$), and

$$M_1 = \int_{R_0}^R 4\pi r^2 \, dr \, \rho_{\text{ext}}(r) = M_0 \left(\frac{3 - k_0}{3 - k_1} \right) a(\tilde{R}^{3-k_1} - 1). \tag{5}$$

According to our simple model,

$$\gamma(\tilde{R} > 1) = \gamma_4 \left[\psi^2 + \left(\frac{17 - 4k_0}{17 - 4k_1} \right) a(\tilde{R}^{3-k_1} - 1) \right]^{-1/2}. \tag{6}$$

Fig. 1 shows a comparison of our simple analytic expression with the results of a hydrodynamic simulation (see Appendix A for the simulation details). It depicts the forward shock Lorentz factor as a function of radius for a spherical ultra-relativistic blast wave that propagates into three different density profiles of the external medium that are described by equation (1). Two of the density profiles are uniform both below and above R_0 ($k_0 = k_1 = 0$) with density jumps of $a = 10$ and 100 at R_0. The third density profile presents a wind termination shock, for which $k_0 = 2$, $k_1 = 0$, and $a = 4$. Fig. 1 demonstrates that despite the simplicity of our analytic approximation, it provides an excellent description of the accurate solution.

Once the reverse shock reaches $\chi \gtrsim 2$, it samples most of the energy in the BM radial profile. At this stage a good fraction of the total energy is already in region 2, and a similar energy is in region 3. A rough estimate for the radius, $R_1 = R_0 + \Delta R$, at which this

---

[2] For convenience, we work throughout this paper in dimensionless variables. Unless specified otherwise, $\tilde{x} \equiv x/x(R_0)$.

occurs may be obtained by using the conditions in region 2 that have been calculated above according to the shock jump conditions for a uniform shell, and checking when most of the energy will be in region 2. This occurs after a mass $\approx \psi^2 M_0$ is swept from $r > R_0$, that is, when the two terms in equation (6) become comparable, which corresponds to $(\tilde{R}^{3-k_1} - 1) = a^{-1}\psi^2[(17-4k_1)/(17-4k_0)] \sim a^{-1/2}$, or

$$\tilde{R}_1 = \left[1 + \frac{\psi^2}{a}\left(\frac{17-4k_1}{17-4k_0}\right)\right]^{1/(3-k_1)}. \tag{7}$$

For $a \gg 1$ this simplifies to $\Delta R/R_0 \approx a^{-1/2}\sqrt{3}(17-4k_1)/[2(17-4k_0)(3-k_1)] \sim a^{-1/2} \ll 1$. Once $E/\gamma^2 c^2 = C_0\psi^2 M_0 + C_1 M_1 = M_{\text{eff}}$ becomes comparable to the mass that would have been swept up at the same radius if the outer density profile was valid everywhere, $4\pi A_1 R^{3-k_1}/(3-k_1)$, the dynamics approach the new BM self-similar solution for $(A, k) = (A_1, k_1)$. By this time $M_{\text{eff}}(R)$ is dominated by the second term in equation (4), and therefore the new BM solution is approached when $\tilde{R}^{3-k_1} - 1$ becomes comparable to $\tilde{R}^{3-k_1}$, that is, when $\tilde{R} \gtrsim \tilde{R}_{\text{BM}} = 2^{1/(3-k_1)}$.

3.2 The resulting light curve

Here the simplified description of the hydrodynamics presented above is used in order to obtain a semi-analytic expression for the resulting light curve. We obtain explicit expressions for the three most relevant PLSs of the synchrotron spectrum: $\nu < \nu_m < \nu_c$, $\nu_m < \nu < \nu_c$, and $\nu > \max(\nu_m, \nu_c)$, where ν_m is the typical synchrotron frequency and ν_c is the cooling frequency. The first two PLSs appear in the slow-cooling regime ($\nu_m < \nu_c$) while the last PLS also appears in the fast-cooling regime ($\nu_m > \nu_c$).

Two useful time-scales for calculating the observed radiation are the radial time, $T_r(R) = t - R/c$, and the angular time, $T_\theta(R) = R/2c\gamma^2$. The radial time is the arrival time of a photon emitted at the shock front at radius R along the line of sight (at $\theta = 0$) relative to a photon emitted at $t = 0$ at $R = 0$. The angular time is the arrival time of a photon emitted at the shock front at an angle of $\theta = \gamma^{-1}$ from the line of sight relative to a photon emitted at the shock front at the same radius R along the line of sight. For convenience, we normalize the observed time by $T_0 = T_r(R_0) = R_0/4(4 - k_0)c\gamma_4^2$, $\tilde{T} \equiv T/T_0$. In our simple model, the radial and angular times are given by

$$\tilde{T}_r(\tilde{R} > 1) = 1 + \left[\psi^2 - \left(\frac{17-4k_0}{17-4k_1}\right)a\right](4 - k_0)(\tilde{R} - 1)$$
$$+ \left(\frac{4-k_0}{4-k_1}\right)\left(\frac{17-4k_0}{17-4k_1}\right)a(\tilde{R}^{4-k_1} - 1), \tag{8}$$

$$\tilde{T}_\theta(\tilde{R} > 1) = 2(4 - k_0)\tilde{R}\left[\psi^2 + \left(\frac{17-4k_0}{17-4k_1}\right)a\left(\tilde{R}^{3-k_1} - 1\right)\right], \tag{9}$$

while

$$\tilde{T}_r(\tilde{R} < 1) = \tilde{R}^{4-k_0}, \quad \tilde{T}_\theta(\tilde{R} < 1) = 2(4 - k_0)\tilde{R}^{4-k_0}. \tag{10}$$

Following Nakar & Piran (2003), we express the observed flux as an integral over the radius R of the forward shock. It is convenient to express the integrand, which represents the contribution from a given radius R to the observed flux at a given observed time T, as the product of two terms:[3] the total emissivity (per unit frequency) of

the blast wave between R and $R + dR$, $A_\nu(R)$, and a weight function, $g(\tau, \beta)$, where $\beta = d\log F_\nu/d\log\nu$ is the spectral slope, which takes into account the relative contribution from a given radius R to the observed flux at a given observed time T:

$$\tilde{F}_\nu(\tilde{T}) = C(\beta) \int_0^{\tilde{R}_{\max}(\tilde{T})} d\tilde{R}\ \tilde{A}_\nu\ g(\tau, \beta). \tag{11}$$

For convenience, all variables are normalized by their value at T_0 or R_0: $\tilde{F}_\nu(\tilde{T}) \equiv F_\nu(T = \tilde{T}T_0)/F_\nu(T_0)$ and $\tilde{A}_\nu(\tilde{R}) \equiv A_\nu(R = \tilde{R}R_0)/A_\nu(R_0)$. The normalization constant $C(\beta)$ may be obtained by the requirement that $\tilde{F}_\nu(\tilde{T} = 1) = 1$, while $\tilde{R}_{\max}(\tilde{T})$ is given by $T_r[\tilde{R}_{\max}(\tilde{T})] = \tilde{T}$ and may be obtained by inverting equation (8) for $\tilde{R}$. The weight function $g(\tau, \beta)$ depends on the the dimensionless 'time' variable

$$\tau(\tilde{R}, \tilde{T}) \equiv \frac{\tilde{T} - \tilde{T}_r(\tilde{R})}{\tilde{T}_\theta(\tilde{R})}, \tag{12}$$

and on the PLS where the observed frequency ν is in, which is specified by the value of the spectral index β ($F_\nu \propto \nu^\beta$). In principle, during the self-similar phase, for $\nu < \nu_c$, g has a complicated form and it also depends on the power-law index, k, of the external density (Nakar & Piran 2003). However, the whole approach that is adopted here (of separating the integrand into the product of A_ν and a relatively simple g where the time dependence is only through τ) is anyway not strictly valid during the non-self-similar phase. Therefore, we choose to use the simplest expression of g at all PLSs, which is the expression obtained in the thin emitting-region approximation (which is accurate for $\nu > \nu_c$):

$$g(\tau, \beta) = (1 + \tau)^{\beta-2}. \tag{13}$$

An approximation for $\tilde{A}_\nu(\tilde{R})$ is obtained by considering three different phases of emission: $\tilde{R} < 1$, $1 < \tilde{R} < \tilde{R}_1$, and $\tilde{R} > \tilde{R}_1$ (similar to the approach taken by Pe'er & Wijers 2006). For $\tilde{R} < 1$ the blast wave is self-similar and $\tilde{A}_\nu(\tilde{R} < 1)$ is similar to the one calculated in Nakar & Piran (2003):

$$\tilde{A}_\nu(\tilde{R} < 1) = \begin{cases} \tilde{R}^{1-k_0} & \nu < \nu_m < \nu_c, \\ \tilde{R}^{2-3p+k_0(3p-5)/4} & \nu_m < \nu < \nu_c, \\ \tilde{R}^{1-3p+k_0(3p-2)/4} & \nu > \max(\nu_m, \nu_c). \end{cases} \tag{14}$$

For $1 < \tilde{R} < \tilde{R}_1$ the reverse shock is crossing the hot BM shell and $\tilde{A}_\nu$ is approximated by evaluating the contribution from the three emitting regions: $\tilde{A}_{\nu,2}$ – the shocked external medium originating from $R > R_0$, $\tilde{A}_{\nu,3}$ – the portion of the BM shell that has been shocked by the reverse shock, and $\tilde{A}_{\nu,4}$ – the unperturbed portion of the BM solution which has not yet been crossed by the reverse shock.

Regions 2 and 3 can be approximated as being uniform with the Lorentz factor given by equation (6). For a relativistic reverse shock, which occurs for a large density bump ($a \gg 10$), we have $\psi \approx (3a/4)^{1/4} \sim a^{1/4}$. The ratio of the density behind the forward shock, $n_2 \approx 4\gamma_3 n_1$, to that behind the reverse shock, $n_3 \approx 4(\gamma_4/2\gamma_3)4\gamma_4 n_0 = 8(\gamma_4^2/\gamma_3)n_0$, is $n_2/n_3 \approx a/2\psi^2 \approx \sqrt{a/3} \sim a^{1/2}$. Since when both shocks are relativistic the velocity of both shocks relative to the contact discontinuity is the same, $c/3$, the width and the volume of regions 2 and 3 are the same (in the contact discontinuity rest frame), so that their (proper) density ratio is also the ratio of the rest mass and the total number of electrons N_e in the two shocked regions. Since $\nu_m \propto \gamma B\gamma_m^2$ and $\gamma_m \propto e/n$ where $e_2 = e_3$ we have $\gamma_{m2}/\gamma_{m3} = n_3/n_2 \approx \sqrt{3/a} \sim a^{-1/2}$ and $\nu_{m2}/\nu_{m3} \approx 3/a \sim a^{-1}$, where $B \propto \epsilon_B^{1/2} e^{1/2}$ is the magnetic field measured in the fluid rest

---

[3] This separation is accurate during the self-similar phase (see Nakar & Piran 2003) and serves here as a useful approximation.

frame and it is assumed that the fraction of the internal energy in the magnetic field, $\epsilon_B = B^2/8\pi\, e$, is the same everywhere. More generally, for any value of $a > 1$, we have

$$\left(\frac{n_3}{n_4}\right)^2 = \frac{a(3a + \psi^2)}{\psi^2(a + 3\psi^2)}, \quad \frac{n_2}{n_4} = \frac{a}{\psi}, \tag{15}$$

and therefore

$$\frac{\nu_{m3}}{\nu_{m2}} = \left(\frac{n_2}{n_3}\right)^2 = \frac{a(a + 3\psi^2)}{3a + \psi^2} \equiv \zeta. \tag{16}$$

Since $F_{\nu,\max} \propto \gamma B N_e$ we have $F_{\nu,\max3}/F_{\nu,\max2} = n_3/n_2 = \zeta^{-1/2} \approx \sqrt{3/a} \sim a^{-1/2}$. Therefore, for $\nu < \nu_m < \nu_c$ or $\nu_m < \nu < \nu_c$, $F_\nu \propto F_{\nu,\max} \nu_m^{\hat{m}}$ and

$$\frac{\tilde{A}_{\nu,3}}{\tilde{A}_{\nu,2}}(1 < \tilde{R} < \tilde{R}_1) = \left(\frac{n_2}{n_3}\right)^{2\hat{m}-1} = \zeta^{\hat{m}-1/2}. \tag{17}$$

For $\nu > \max(\nu_m, \nu_c)$ the ratio of the spectral emissivity between regions 2 and 3 is equal to the ratio of the energy flux through the forward and reverse shocks, respectively, that goes into electrons with a synchrotron frequency close to the observed frequency, $\nu_{\mathrm{syn}}(\gamma_e) \sim \nu$. Since the magnetic field in the two regions is similar and so is the total energy flux,[4] the same electron Lorentz factor γ_e is required for $\nu_{\mathrm{syn}}(\gamma_e) \sim \nu$, and

$$\frac{\tilde{A}_{\nu,3}}{\tilde{A}_{\nu,2}}(1 < \tilde{R} < \tilde{R}_1) = \left(\frac{\gamma_{m,3}}{\gamma_{m,2}}\right)^{p-2} = \zeta^{(p-2)/2} \qquad \nu > \max(\nu_m, \nu_c). \tag{18}$$

Region 4 contributes only to $\nu < \nu_c$. The conditions in this region still follow the BM solution, since it does not yet know about the density jump, but the fraction of the BM profile that has still not passed through the reverse shock decreases with time. This fraction, f, is 1 at $\tilde{R} = 1$ and ~ 0 at $\tilde{R}_1$. We parametrize $f(\tilde{R})$ using a linear transition with radius:

$$f(\tilde{R}) = \frac{\tilde{R}_1 - \tilde{R}}{\tilde{R}_1 - 1}. \tag{19}$$

Summing the contributions from all the different regions and evaluating the contribution from region 2 as $F_\nu \propto F_{\nu,\max} \nu_m^{\hat{m}} \propto M^{\hat{M}} \gamma^{\hat{\gamma}} \rho_{\mathrm{ext}}^{\hat{\rho}} R^{\hat{r}}$, we obtain

$$\tilde{A}_\nu(1 < \tilde{R} < \tilde{R}_1)g(\tau, \beta) = \Theta(\nu_c - \nu)f(\tilde{R})\tilde{A}_{\nu,\tilde{R}<1}(\tilde{R})g_{\tilde{R}<1}(\tau, \beta)$$

$$+ a^{\hat{\rho}} \tilde{R}^{\hat{r}-1-k_1\hat{\rho}} \left(1 + \zeta^{\hat{m}-1/2}\right) \left[\frac{3 - k_0}{3 - k_1} a\left(\tilde{R}^{3-k_1} - 1\right)\right]^{\hat{M}}$$

$$\times \left[\psi^2 + \frac{17 - 4k_0}{17 - 4k_1} a\left(\tilde{R}^{3-k_1} - 1\right)\right]^{-\hat{\gamma}/2} g_{\tilde{R}>1}(\tau, \beta), \tag{20}$$

where $\Theta(x)$ is the Heaviside step function, and the values of the exponents for the relevant PLSs are given in Table 1. The subscript $\tilde{R} < 1$ or $\tilde{R} > 1$ means that the expressions for these $\tilde{R}$ values should be used, even if the actual value of $\tilde{R}$ does not fall within this range.

At the third phase, $R > R_1$, the reverse shock has finished crossing the hot BM shell so that only regions 2 and 3 contribute to the emission. Region 2 gradually relaxes into a self-similar profile, while

Table 1. The values of the exponents in equations (20) and (21) for different PLSs of the spectrum.

PLS	$\hat{M}$	$\hat{r}$	$\hat{m}$	$\hat{\gamma}$	$\hat{\rho}$
$\nu < \nu_m < \nu_c$	1	0	$-1/3$	$2/3$	$1/3$
$\nu_m < \nu < \nu_c$	1	0	$(p-1)/2$	$2p$	$(p+1)/4$
$\nu > \max(\nu_m, \nu_c)$	0	2	$(p-1)/2$	$2p$	$(p+2)/4$

region 3 expands and cools at its tail. The contribution from region 2 remains the same as in the previous phase (i.e. at $R_0 < R < R_1$). Region 3 does not contribute at $\nu > \nu_c$, while below ν_c its contribution can be approximated by assuming that its hydrodynamic evolution follows that of a fluid element within the tail of the BM profile, for which $\nu_m(\chi)/\nu_m(\chi = 1) = \chi^{-(37-5k_1)/6(4-k_1)}$ and the peak spectral emissivity per electron scales as $P_{\nu,e,\max}(\chi)/P_{\nu,e,\max}(\chi = 1) = \chi^{-(29-7k_1)/6(4-k_1)}$. Since during the self-similar evolution $\chi \propto R^{4-k_1}$ while the number of emitting electrons in region 3 is constant ($N_e = M_0/m_p$), we obtain

$$\tilde{A}_\nu(\tilde{R} > \tilde{R}_1) = a^{\hat{\rho}} \tilde{R}^{\hat{r}-1-k_1\hat{\rho}} \left[\psi^2 + \frac{17 - 4k_0}{17 - 4k_1} a\left(\tilde{R}^{3-k_1} - 1\right)\right]^{-\hat{\gamma}/2}$$

$$\times \left\{\frac{3 - k_0}{3 - k_1} a\left[\tilde{R}^{3-k_1} - 1 + \left(\tilde{R}_1^{3-k_1} - 1\right)\zeta^{\hat{m}-1/2}\left(\frac{\tilde{R}}{\tilde{R}_1}\right)^{\hat{\mu}}\right]\right\}^{\hat{M}}, \tag{21}$$

where

$$\hat{\mu} = -\frac{1}{6}\left[29 - 7k_1 + \hat{m}(37 - 5k_1)\right], \tag{22}$$

and the power-law indices for the three different PLSs are listed in Table 1.

4 CASE STUDIES OF SPHERICALLY SYMMETRIC JUMPS IN THE EXTERNAL DENSITY

In this section, we study two spherically symmetric external density profiles which are of special interest for GRB afterglows: a wind termination shock, and a density jump in a uniform medium.

4.1 A wind termination shock

The semi-analytic model for the light curve that has been developed in Section 3.2 is now applied to a wind termination shock, for which $k_0 = 2$, $k_1 = 0$, and $a = 4$. We also compare the results of this semi-analytic model to the numerical model that is described in Appendix A.[5] The resulting light curves are displayed in Figs 2–4 for the three most relevant PLSs of the spectrum. The results of the semi-analytic model nicely agree with the numerical results. Some differences do exist but the qualitative behaviour (i.e. variation time-scales and amplitudes) is similar, and even the quantitative differences are not very large. The main differences between the semi-analytic model and the numerical simulations are a small initial dip before the rise in the flux for $\nu < \nu_c$, a difference in the exact starting time for the change in the temporal decay index for $\nu_m < \nu < \nu_c$ and $\nu > \max(\nu_m, \nu_c)$, and a slightly different normalization of the asymptotic flux at $T \gg T_0$ for $\nu < \nu_c$. The latter arises since we neglect the dependence

---

[4] The energy flux is equal in the limit of a relativistic reverse shock, where the velocities of both shocks relative to regions 2 and 3 are the same ($c/3$). However, even in the limit of a Newtonian reverse shock ($a - 1 \ll 1$) the velocity of the reverse shock relative to region 3 approaches $c/\sqrt{3}$ (the sound speed) which is only a factor of $\sqrt{3}$ larger than the velocity of the forward shock relative to region 2 ($c/3$).

[5] This code assumes optically thin synchrotron emission and does not take into account opacity-related effects such as synchrotron self-absorption or synchrotron self-Compton.
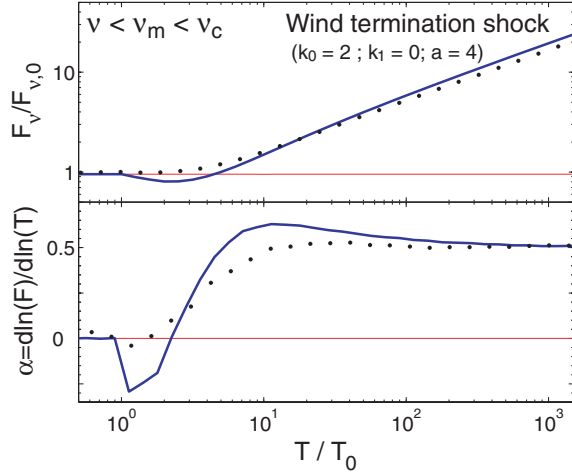
Figure 2. The light curve (upper panel) and the evolution of the temporal decay index α (lower panel) for the synchrotron emission from a spherical relativistic blast wave running into a wind termination shock ($k_0 = 2$, $k_1 = 0$, $a = 4$ in equation 1), in the frequency range $\nu < \nu_m < \nu_c$. Shown are the results of the semi-analytic model described is Section 3.2 (solid thick blue line) and of the numerical code described in Appendix A (black dots) for a wind termination shock. The semi-analytic result for the same wind without a termination shock (where $\rho_{ext} = A_0 r^{-k_0}$ at all radii; red thin line) is added for reference.
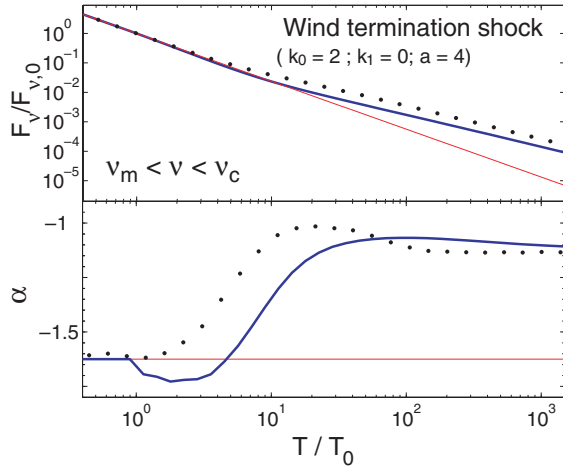
Figure 3. Same as Fig. 2 but for the spectral range $\nu_m < \nu < \nu_c$. We use $p = 2.5$.

of the function g on k in these PLSs (g does not depend on k for $\nu > \nu_c$) in the semi-analytic model. This causes a deviation (by a factor of the order of unity) in the normalization of the asymptotic flux calculated by the semi-analytic model, compared to its true value, in cases where $k_0 \neq k_1$.

The light curves show a smooth transition between the asymptotic power-law behaviour at $T < T_0$ and at $T \gg T_0$. There is no rebrightening in PLSs where the flux decays at $T < T_0 (\nu > \nu_m)$, and no sharp feature in the light curve which might serve as a clear observational signature. The transition between the two asymptotic curves ($T < T_0$ & $T \gg T_0$) is continuous with the temporal decay index rising slowly for $\nu < \nu_c$ and mildly fluctuating for $\nu > \nu_c$. The values of the temporal index $\alpha \equiv d \log F_\nu / d \log T$ during its rising or fluctuating phase do not exceed its asymptotic value at $T \gg T_0$
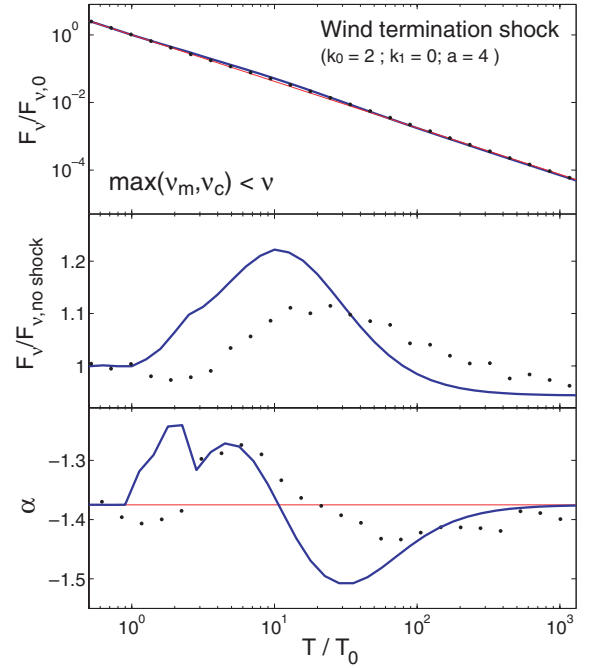

Figure 4. Same as Fig. 3 but for the spectral range $\nu > \max(\nu_m, \nu_c)$, and with an additional panel for the ratio of the flux with and without a wind termination shock.

by more than 0.1 at any time. Therefore, the only observable signature of a wind termination shock is a continuous break (with $\Delta\alpha = 0.5$) below ν_c. Above ν_c there is no change in the asymptotic value of the temporal index α, and it only slowly fluctuates with a very small amplitude (≈ 0.1), which is extremely hard to detect. Note that these results are applicable for a case where the blast wave remains relativistic also after it encounters the termination shock (i.e. $\gamma_3 \approx 0.72 \gamma_4 \gtrsim 3$).

The break in the light curve (the shallowing of the flux decay for $\nu_m < \nu < \nu_c$ or the transition from constant to rising flux for $\nu < \nu_m < \nu_c$) occurs over about one decade in time. Initially, there is very little difference relative to the case where there is no wind termination shock (and $\rho_{ext} = A_0 r^{-k_0}$ at all radii), or even a small dip at $\nu > \max(\nu_m, \nu_c)$, while a rise in the *relative* flux starts at $\tilde{T} = T/T_0 \sim 2 - 4$. The light curve approaches its asymptotic late-time power-law behaviour at about $\tilde{T} \sim 10 - 10^2$. This can be understood as follows.

The contribution to the observed flux from within a given angle θ around the line of sight does not change drastically across the density jump. However, there is a sudden decrease in the Lorentz factor of the shocked material behind the forward shock, so that the effective visible region increases from $\theta \lesssim \gamma_4^{-1}$ to $\theta \lesssim \gamma_3^{-1} = \psi/\gamma_4$. This is responsible for most of the observable signature, and it starts affecting the light curve notably only when photons emitted just after R_0 from an angle $\theta \gtrsim \gamma_4^{-1}$ arrive to the observer, namely at $\sim T_\theta(R_{0,-}) = 4T_0$ where

$$T_\theta(R_{0,\pm}) \equiv \lim_{\epsilon \to 0} T_\theta[(1 \pm \epsilon)R_0]. \tag{23}$$

This full angular effect becomes apparent when photons from the same radius and an angle of $\theta \sim \gamma_3^{-1}$ reach the observer, at $\sim T_\theta(R_{0,+}) = 2(4 - k_0)\psi^2 T_0 \approx 8T_0$. The radial time is smaller than the angular time, and therefore the radial effect would only slightly increase the time when the total effect becomes prominent. The light curve approaches its asymptotic power-law behaviour when

the dynamics approach the new self-similar evolution, at $\sim \tilde{R}_{BM} = 2^{1/(3-k_1)}$. Since $[\gamma_4/\gamma(\tilde{R}_{BM})]^2 \sim 4$ and therefore $\tilde{T}_\theta(\tilde{R}_{BM}) \sim 16$, while $\tilde{T}_r(\tilde{R}_{BM}) \sim 2.6$, this corresponds to $\tilde{T} \sim 20$. Obviously, this is a rough estimate, but it agrees reasonably well with the numerical results.

Our main conclusion is that the encounter of a relativistic, adiabatic blast wave with a wind termination shock does not produce a prominent, readily detectable, signature in the light curve. This differs from the conclusions of previous computations that explored the light curves resulting from wind termination shocks (Ramirez-Ruiz et al. 2001b, 2005; Dai & Lu 2002; Eldridge et al. 2006; Pe'er & Wijers 2006). The earlier discussions predicted a clear observational signature, including an optical rebrightening, even in cases when the termination shock happens at a sufficiently small radius, at which the blast wave is still relativistic as it runs into it. In some of the earlier works (Ramirez-Ruiz et al. 2001b, 2005), the termination shock is placed at a large radius so the blast wave becomes non-relativistic after hitting the density jump, whereas our conclusions are valid for the case where the forward shock remains fully relativistic after encountering the density jump. This can account for some of the differences in the predicted light curves. Other works *did* assume that the shock wave stays relativistic throughout (Dai & Lu 2002; Eldridge et al. 2006; Pe'er & Wijers 2006). In these cases, our light curves are different because we explicitly take into account the impact of the reverse shock on the dynamics, and properly account for the dependence of the photon arrival times on the angle relative to the line of sight. Both effects tend to smooth the variability in the resulting light curve.

4.2 Spherical jump in a uniform external medium

Next we explore the light curve that results from a spherical relativistic blast wave running into a uniform external density with a jump at some radius R_0 (i.e. $k_0 = k_1 = 0$ and $a > 1$). Such a density profile can be generated, for example, by the contact discontinuity between shocked winds from two evolutionary phases of the massive star progenitor. This configuration also serves as an approximation for a large density clump, and constrains the observational signature from a small density clump (see Section 5).

Figs 5–7 depict the light curves from our semi-analytic model (described in Section 3.2) for four different density contrasts ($a = 2, 10, 100, 1000$), as well as the results of the numerical simulation (described in Appendix A) for two of these cases ($a = 10, 100$). The agreement between the semi-analytic model and the results of the simulation is satisfactory. In all cases (all the different PLSs and a values), the semi-analytic model qualitatively follows the numerical results and recovers the main features (i.e. the correct time-scales and amplitudes of the variations and their derivatives). In most cases, the quantitative comparison is also impressive (better than 10 per cent). The main differences between the semi-analytic model and the simulation results are the small initial dip before the rise in the flux for $\nu < \nu_m < \nu_c$ (observed also in the wind termination shock) and an overshoot for $a = 100$ in this PLS. The semi-analytic model predicts an initial dip for $\nu_m < \nu < \nu_c$, which also appears, although less prominently, in the results of the numerical simulations.

The main result that emerges from Figs 5–7 is that no sharp features appear in any of the light curves, no matter how high the density contrast [at least as long as $\gamma_3 = \gamma_4/\psi \gg 1$ where $\psi \approx (3a/4)^{1/4}$ for $a \gg 1$]. Moreover, the maximal deviation of the temporal decay index, α, from its asymptotic value (which is the same for $T < T_0$ and $T \gg T_0$, since $k_0 = k_1$) is not large (<1 in all PLSs
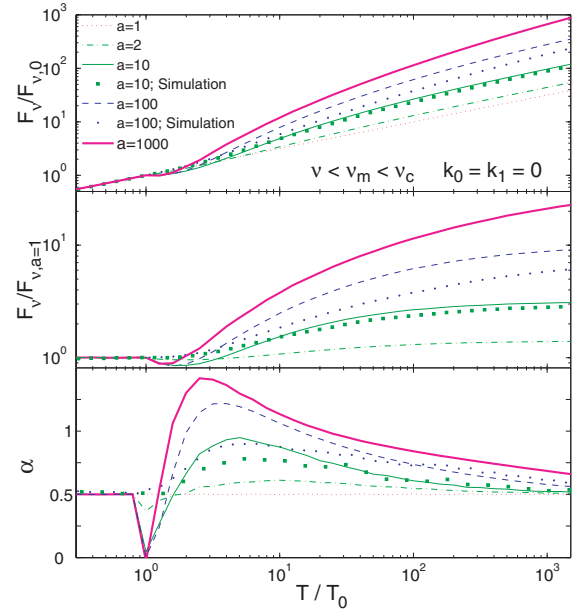

Figure 5. The light curve (upper panel), the ratio of the flux with and without a density jump (middle panel), and the evolution of the temporal index α (lower panel) for the synchrotron emission from a spherical relativistic blast wave propagating into a medium with a step-like density profile ($k_0 = k_1 = 0$ in equation 1), in the frequency range $\nu < \nu_m < \nu_c$. Shown are the results of the semi-analytic model described is Section 3.2 for four different density contrasts ($a = 2, 10, 100$ and 1000) and of the numerical code described in Appendix A for two cases ($a = 10$ and 100). We use here $p = 2.5$.
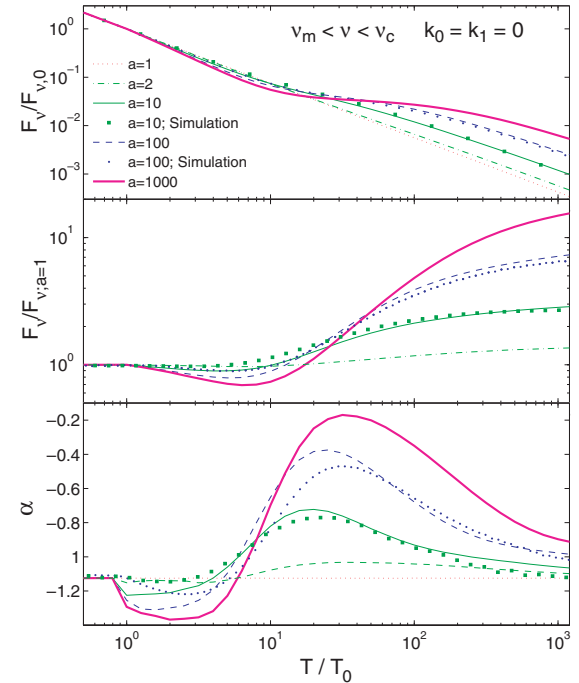

Figure 6. Same as Fig. 5 but for the spectral range $\nu_m < \nu < \nu_c$.

at all times), and as we show for $\nu_m < \nu < \nu_c$ it approaches an asymptotic value at large a.

Observationally, the most interesting PLS is $\nu_m < \nu < \nu_c$, since it typically includes the optical. In this PLS the flux enhancement,
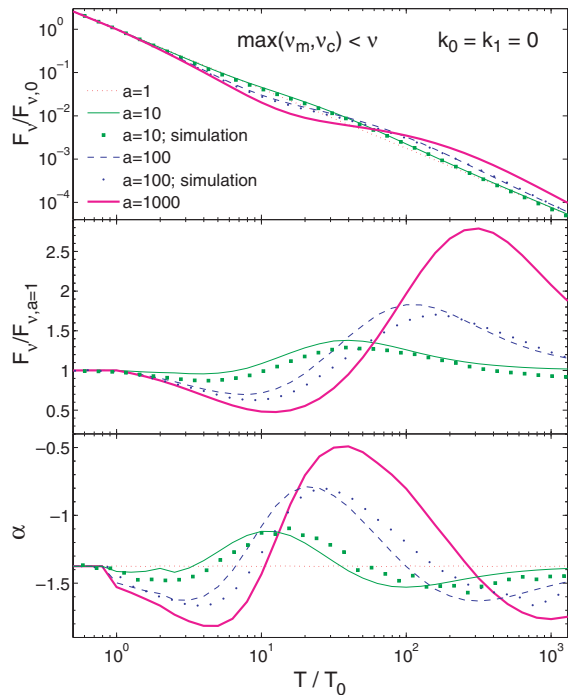
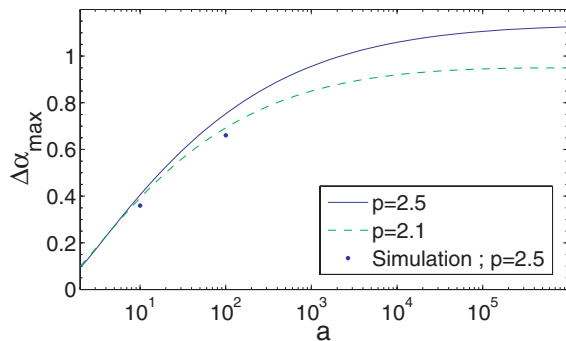**Figure 7.** Same as Fig. 5 but for the spectral range ν_m, $\nu_c < \nu$. For clarity, we omitted the $a = 2$ curve.

Figure 8. The maximal deviation of the temporal index ($\alpha \equiv \mathrm{d}\log F_\nu / \mathrm{d}\log T$) from its asymptotic value, $\Delta\alpha_{\max}$, as a function of the density contrast a, for electron power-law indices $p = 2.5$ (solid line) and $p = 2.1$ (dashed line). The results of the numerical simulations for $a = 10$ and 100 (in which $p = 2.5$) are marked as the dots.

$f(T) \equiv F_\nu(T)/F_\nu(T, a = 1)$, is asymptotically $f(T \gg T_0) = a^{1/2}$, but the transition to this asymptotic value is very gradual. Fig. 8 depicts the value of the maximal deviation of the temporal index α from its asymptotic value, $\Delta\alpha_{\max}$, as a function of a for two values of p. We emphasize the behaviour of $\Delta\alpha$ since it is perhaps the easiest quantity to observe. The inability of density fluctuations to produce sharp features in the light curve is demonstrated by the low values of $\Delta\alpha_{\max}$ that we find. Some examples are 0.1, 0.4 (0.35), 0.75 (0.65) and 0.95 for $a = 2, 10, 100$ and 1000, respectively, where the values in brackets correspond to the results of the numerical simulation. Furthermore, for very large values of a, $\Delta\alpha_{\max}$ saturates at a value of ≈ 1. Since $\alpha(T < T_0) = -3(p - 1)/4 \sim -1$, no rebrightening (i.e. $\alpha > 0$) is observed. Moreover, at first (just after T_0) a mild dip, is apparent in the light curve. The depth of this dip increases with a. Another constraining observable is the time over which $\Delta\alpha_{\max}$

is obtained. Thus, we consider the ratio of the time when $\Delta\alpha_{\max}$ is obtained and the time when $\Delta\alpha > 0$ once it recovers from its initial dip. We find this time ratio to be ≈ 5 for any reasonable values of a and p.

Our results can be understood as follows. The contribution to the emission per unit area of the shock front along the line of sight, from a radius R to an observer time T, increases with the energy density of the shocked fluid and with its bulk Lorentz factor. A density jump immediately increases the energy density of the freshly shocked fluid (by a factor $a\psi^{-2} > 1$) while reducing its Lorentz factor (by a factor $\psi^{-1} < 1$). The net effect is such that the decrement in the Lorentz factor dominates by a small margin, and the line-of-sight emission actually drops at R_0. This drop increases with a and is the source of the observed dip right after T_0. The same drop in γ is also the origin of the flux increase that follows. With a lower γ the largest angle θ (from the line of sight) that contributes to the observed emission increases. This contribution becomes apparent only when emission from $\theta \gtrsim 1/\gamma_4$ arrives to the observer, at $\sim T_\theta(R_{0,-}) = 8T_0$, and is completed when emission from $\theta \gtrsim 1/\gamma_3$ is observed, at $\sim T_\theta(R_{0,+}) = \psi^2 T_\theta(R_{0,-}) \sim a^{1/2} T_\theta(R_{0,-})$. The transition to the asymptotic value continues up to $T_{\mathrm{BM}} \sim a^{1/2} T_\theta(R_{0,+}) \sim 10aT_0$. These time-scales explain why the transition is so gradual, and so is the convergence of α to its asymptotic value at $T \gg T_0$, for large a. Our results show that the maximal value of α is observed around $T_\theta(R_{0,+})$, and that for $a \gg 1$, $f[T_\theta(R_{0,+})] \approx (0.1 - 0.4)\,a^{1/2}$. Now $\Delta\alpha$ can be approximated by $\log\{f[T_\theta(R_{0,+})]\}/\log[T_\theta(R_{0,+})/T_\theta(R_{0,-})]$ which approaches 1 at large a.

It is generally accepted that the main signature of density fluctuations in the external medium are chromatic fluctuations in the afterglow light curve, where sharp features are expected below ν_c (which typically includes the optical bands) and no (or very weak) variability is expected above ν_c (which typically includes the X-rays). This conclusion relies on the fact that a change in the external density effects the asymptotic light curve (at $T \gg T_0$ compared to $T < T_0$) only below ν_c, but not above ν_c. A comparison between Figs 6 and 7 shows that while the behaviour in these two PLSs is indeed different, the general concept described above is inaccurate and the differences are more subtle. Both PLSs show smooth fluctuations in the temporal index α with a *comparable* amplitude. The main difference is in the flux normalization of the asymptotic light curve at $T \gg T_0$ compared to $T < T_0$. Above ν_c the asymptotic light curve does not change and the observed flux fluctuates around this asymptotic power-law decay, while below ν_c the normalization for the asymptotic light curve at $T \gg T_0$ is larger than that at $T < T_0$ by a factor of $a^{1/2}$, and therefore the flux continuously increase *relative* to the case where there is no density jump ($a = 1$). This type of difference in the behaviour is, however, much harder to detect (compared to variations in α) since, obviously, the reference light curve (for $a = 1$) cannot be observed.

Previous works have explored the light curves arising from the propagation of a relativistic, adiabatic, spherical blast wave in such a density profile (Dai & Lu 2002; Lazzati et al. 2002; Nakar et al. 2003; Nakar & Piran 2003). These works predicted sharper features with an observable rebrightening at $\nu_m < \nu < \nu_c$ (i.e. $\alpha > 0$) which does not exist in the results presented here. As in the case of a wind termination shock, the difference between the results arises from the fact that our calculation considers both the effects of the reverse shock on the dynamics and the dependence of the photon arrival times on the angle from the line of sight. Taking into account the effects of the reverse shock on the dynamics makes a difference also when a mild density jump is considered since as we show here even when $a \sim 2$ its effect on the dynamics cannot be neglected.
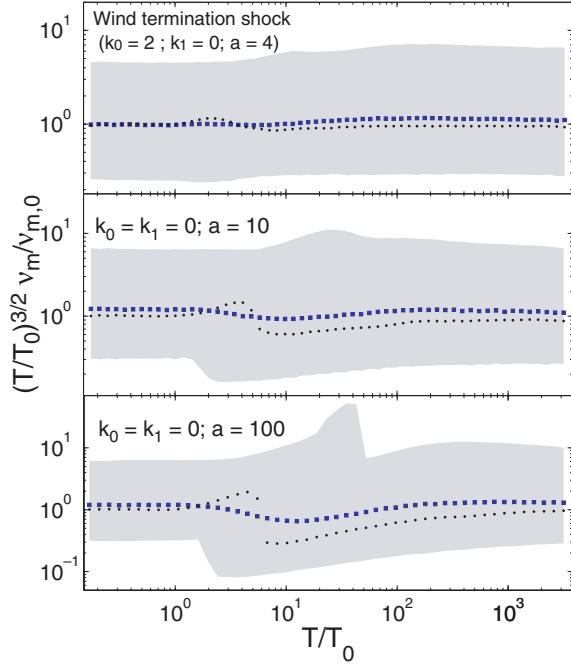
Figure 9. The temporal evolution of the typical synchrotron frequency ν_m (dotted line), which is defined as the frequency at which the spectral index β is mid-way between its value at $\nu \ll \nu_m$ ($\beta_1 = 1/3$) and at $\nu \gg \nu_m$ [$\beta_2 = (1 - p)/2$], $\beta = (\beta_1 + \beta_2)/2$. We use $p = 2.5$. The shaded region shows the frequency range where 80 per cent of the change in β occurs (between 10 and 90 per cent of $\Delta\beta = \beta_1 - \beta_2$). The frequency where the asymptotic power laws well above and below ν_m meet is marked with the filled squares. For clarity, all frequencies are normalized by $\nu_{m,0} = \nu_m(T_0)$ and multiplied by the appropriate power of $\bar{T} = T/T_0$ which takes out the asymptotic time dependence of ν_m at early and late times. The different panels are for different spherical density profiles with a sharp density jump that have been studied in Section 4.1 – a wind termination shock (upper panel), and in Section 4.2 – a spherical density jump by a factor of $a = 10$ (middle panel) and $a = 100$ (lower panel) in a uniform medium.

4.3 The Effects of proximity to a break frequency

So far we have assumed that the observed frequency ν is very far from the break frequencies (ν_m and ν_c) and therefore remains in the same PLS of the synchrotron spectrum throughout the hydrodynamic transitions that we have investigated. Under that assumption, the flux density normalized by its value at T_0 is independent of frequency within each PLS. In this section, we examine the effect on the light curve if the observed frequency is in the vicinity of a break frequency around the time of the hydrodynamic transition. For this purpose, we use our numerical code[6] and consider the cases that have been studied numerically in Section 4.1 (a wind termination shock) and in Section 4.2 (a spherical density jump by a factor of $a = 10$ or 100 in a uniform medium).

Figs 9 and 10 show the temporal evolution of the spectral break frequencies ν_m and ν_c, respectively, around the time of the density jump. The break frequencies are defined as[7] $\nu_b = \min \{\nu | \beta(\nu) < 0.5\beta_1 + 0.5\beta_2\}$, where β_1 and β_2 are the asymptotic values

---

[6] Since our semi-analytic model was designed only for the case where the observed frequency remains in the same PLS, it is not appropriate for this purpose.

[7] Defining instead $\nu_b = \max \{\nu | \beta(\nu) > 0.5\beta_1 + 0.5\beta_2\}$ makes no notable difference.
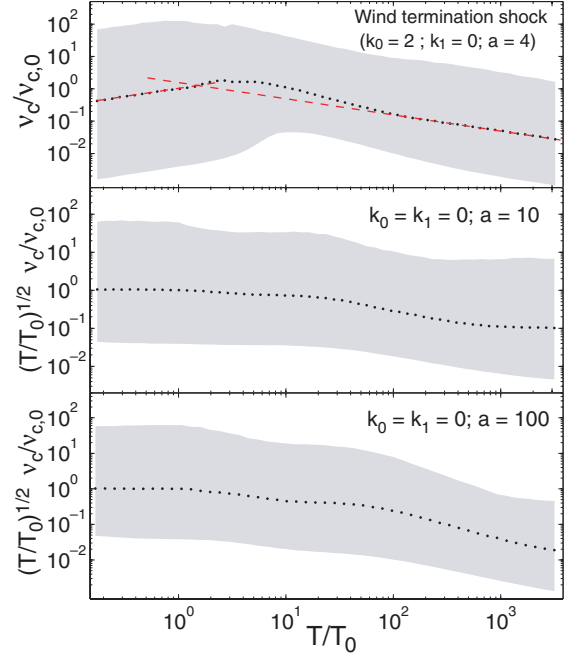

Figure 10. The temporal evolution of the cooling break frequency, ν_c, in the same format as Fig. 9; here $\beta_1 = (1 - p)/2$, $\beta_2 = -p/2$, and again $p = 2.5$. For a wind termination shock (upper panel), the asymptotic temporal index at $T < T_0(\alpha_1 = 1/2$; left-hand dashed line) is different from that at $T \gg T_0(\alpha_2 = -1/2$; right-hand dashed line), and therefore the normalized frequencies are not multiplied by $(T/T_0)^{1/2}$ as in the other two panels (that are for a density jump in a uniform medium for which $\alpha_1 = \alpha_2 = -1/2$).

of the spectral index β at $\nu \ll \nu_b$ and $\nu \gg \nu_b$, respectively, and the subscript b = m and c. The shaded region shows the frequency range ν_{10} per cent $< \nu < \nu_{90}$ per cent where ν_{10} per cent $= \min\{\nu | \beta(\nu) < 0.9\beta_1 + 0.1\beta_2\}$ and ν_{90} per cent $= \max\{\nu | \beta(\nu) > 0.1\beta_1 + 0.9\beta_2\}$, that is, where 80 per cent of the change in β across the spectral break occurs.

The typical synchrotron frequency ν_m fluctuates around its asymptotic $T^{-3/2}$ power-law decay, which does not depend on the power-law index k of the external density. Furthermore, even for a wind termination shock there is no observable change in the asymptotic normalization (i.e. the asymptotic value of $T^{3/2} \nu_m$) and only a very small change in the width of the spectral break which is depicted by the shaded region (in agreement with the semi-analytic results of Granot & Sari 2002). For a density jump in a uniform medium, there is no change in the asymptotic normalization or in the asymptotic shape of the spectral break, again as expected from analytic calculations. Both the amplitude and the typical time-scale of the fluctuations in $T^{3/2} \nu_m$ increase with the density contrast a, where the amplitude scales roughly as $a^{1/2}$ and the time-scale is roughly linear in a. There is a sharp feature in ν_m which occurs first for $\nu_{m,10}$ per cent, then for ν_m, and finally for $\nu_{m,90}$ per cent. This can be understood as follows. Immediately after the forward shock encounters the density jump ν_m decreases in region 2 and increases in region 3, by a factor of $\sim a^{1/2}$ in both cases. Therefore, as long as the region 3 contributes significantly to the observed spectrum, the break is a superposition of two peaks (corresponding to $\nu_{m,2}$ and $\nu_{m,3}$), separated by a factor of $\sim a$ in frequency, and thus its width increases significantly. Moreover, it causes $\beta(\nu)$ to be non-monotonic, and the definitions of $\nu_{m,10}$ per cent, ν_m, and $\nu_{m,90}$ per cent cause these frequencies to have a finite jump when the extremum in $\beta(\nu)$ crosses the appropriate value of β, which occurs later for higher

frequencies. Given the complex structure of the spectral break around ν_m, we also present in Fig. 9 the evolution of the frequency where the asymptotic power laws well above and below the break meet (which can serve as an alternative definition for the location of the break frequency, as was done in Granot & Sari 2002). This frequency evolves very smoothly and shows very mild fluctuations in all cases, since it is less affected by the transient broadening of the spectral break during the hydrodynamic transition.

The evolution of the cooling break frequency, ν_c, is shown in Fig. 10. For a wind termination shock the temporal index α has different asymptotic values at $T < T_0 (\alpha_1 = 1/2)$ and at $T \gg T_0 (\alpha_2 = -1/2)$; ν_c transitions rather smoothly between these two asymptotic limits, with a slight overshoot (i.e. $d \log \nu_c / d \log T$ dips below $-1/2$) due to the increase in density across the jump (the asymptotic value of ν_c decreases with increasing density). The asymptotic behaviour of ν_c is marked with the dashed lines showing that for practical purposes (e.g. analytic calculation) it can be well approximated as a sharp temporal transition between α_1 and α_2 at $T \approx 1.5\, T_0$, while keeping in mind that the spectral break itself is very smooth at any time. For a density jump in a uniform medium, the asymptotic value of the temporal index does not change ($\alpha_1 = \alpha_2 = -1/2$), but the asymptotic normalization of $T^{1/2} \nu_c$ at $T \gg T_0$ is a factor of a lower than at $T < T_0$. The transition between the two asymptotic limits is fairly smooth. The shaded region which corresponds to 80 per cent of the change in β across the break is significantly larger for ν_c than for ν_m, corresponding to a smoother break, in agreement with semi-analytic calculations (Granot & Sari 2002). The transition to the late-time asymptotic behaviour stretches over a larger factor in time, which increases with a.

Figs 11 and 12 show light curves for frequencies that are in the proximity of ν_m and ν_c, respectively, around the time of the density jump. There is a smooth transition between the light curves for frequencies that are well below the break frequency and those for frequencies well above the break frequency around the time of the density jump. Our main conclusions from Sections 4.1 and 4.2 remain valid also when the observed frequency is near a break frequency around the time of the density jump. In particular, there is no rebrightening at $\nu \gg \nu_m$, and the observed features in the light curve are very smooth. Therefore, our main results are rather robust.

5 A CLUMP IN THE EXTERNAL DENSITY

In this section, we estimate the effect of a clump in the external density on the light curve. By a clump we refer to a well localized region of typical size l_{cl} which is overdense by a factor of $a > 1$ relative to the uniform background external density. For a given clump size l_{cl} and overdensity a (well within the clump, near its centre), the effect on the light curve is expected to be larger if the clump has sharper edges, that is, the smaller length-scale Δl over which the density rises by a factor of $\approx a$ relative to the background density. While in practice one might, in many cases, expect $\Delta l \sim l_{cl}$, we consider the limit of a sharp edged clump with $\Delta l \ll l_{cl}$, in order to maximize the effect on the light curve.

Because of relativistic beaming, most of the contribution to the observed light curve from a given radius R is from within an angle of $\theta \lesssim \gamma^{-1}$ around the line of sight, which corresponds to a lateral size of $\sim R/\gamma$. Therefore, a clump in the external density of size[8]

---

[8] Here γ is the Lorentz factor inside the clump, which is smaller than that before the afterglow shock hits the clump, by a factor ψ that is given in equation (3).
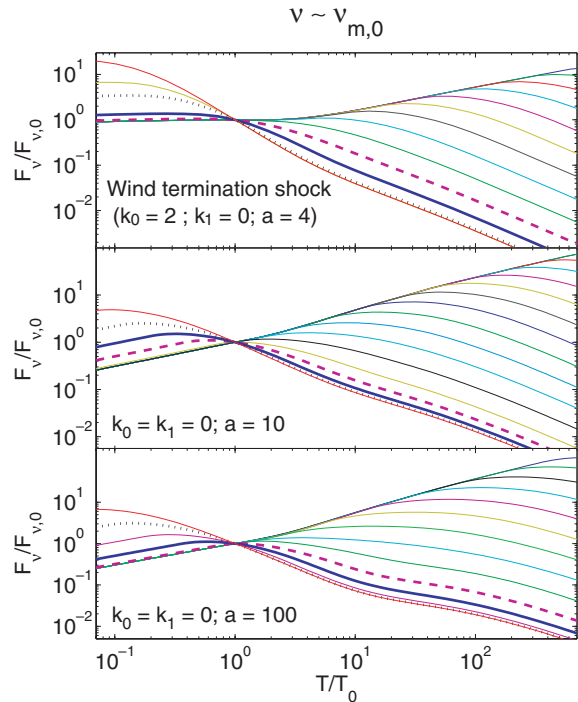

Figure 11. The light curves for frequencies that are in the vicinity of ν_m at the time of the density jump, for the same hydrodynamic transitions that are shown in Fig. 9 (with $p = 2.5$). The solid thick line is for $\nu \approx \nu_m(T_0)$, the dashed thick line is for $\nu \approx \nu_{m,10\, \mathrm{percent}}(T_0)$, and the dotted thick line is for $\nu \approx \nu_{m,90\, \mathrm{per\, cent}}(T_0)$. The remaining curves are spaced by a factor of 2.5 in frequency in the middle panel and by a factor of 3 in the top and bottom panels. Note that since the curves are normalized, those with $\nu \ll \nu_m(T_0)$ overlap at early times and deviate at late times when ν_m drops.

$l_{cl} \gg R/\gamma$ would not differ considerably from a spherically symmetric density jump that was considered in Section 3. If the surface of the clump is not normal to the line of sight (e.g. if the line of sight to the central source does not pass through the centre of a spherical clump), this is expected to reduce the effect of the clump on the light curve (similar to what is expected if the clump does not have very sharp edges, $\Delta l \sim l_{cl}$ rather than $\ll l_{cl}$). Therefore, the results of Section 3 can be viewed as a rough upper limit on the effect of 'big' clumps ($l_{cl} > R_0/\gamma_3$). Small to intermediate clumps, of size $l_{cl} \lesssim R_0/\gamma_3$ are expected to have a smaller effect on the light curve and are investigated below.

The results of the previous section, and in particular the semi-analytic model for the light curve that was derived in Section 3.2, can be used to put an approximate upper limit on the effect that a density clump could have on the observed light curve. Such a limit is achieved by using the spherical model from Section 3.2 within a finite solid angle: $\theta_{min} < \theta < \theta_{max}$ and $\phi_{min} < \phi < \phi_{max}$ in spherical coordinates, while in the radial direction the clump extends out to $R \gg R_0$. In practice we expect the radial extent of the clump to be $\Delta R \sim l_{cl}$, similar to its extent in the θ direction ($\sim R_0 \Delta \theta$ where $\Delta \theta = \theta_{max} - \theta_{min}$) and in the ϕ direction ($\sim R_0 \bar{\theta} \Delta \phi$ where $\Delta \phi = \phi_{max} - \phi_{min}$ and $\bar{\theta} = [\theta_{min} + \theta_{max}]/2$). In our coarse approximation the clump has no upper bound in the radial direction, and its lateral size scales linearly with radius. Obviously, this sets an (approximate) upper limit for the effect on the light curve of a clump with a size l_{cl} in all directions (which is roughly given by $l_{cl} \sim R_0 \Delta \theta \sim R_0 \bar{\theta} \Delta \phi \sim \Delta R$ in spherical coordinates).
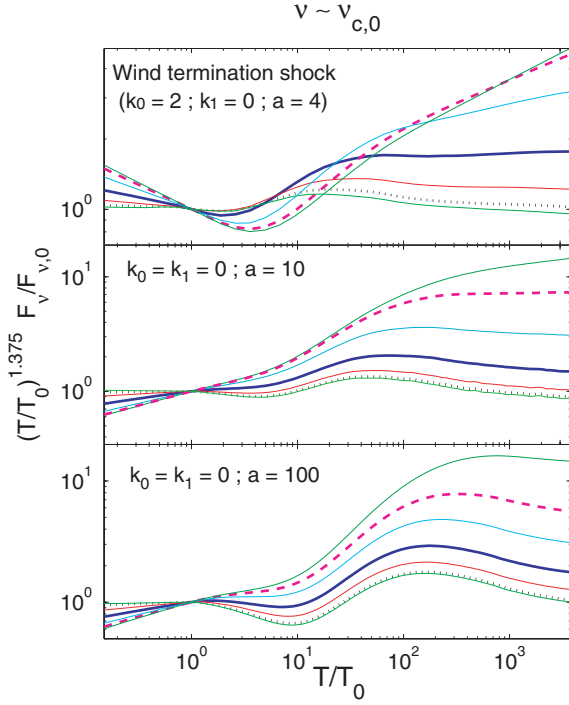
Figure 12. The light curves for frequencies near ν_c at the time of the density jump, for the same hydrodynamic transitions that are shown in Fig. 10 (with $p = 2.5$). The normalized flux is multiplied by $(T/T_0)^{(3p-2)/4} \rightarrow \tilde{T}^{1.375}$ in order to eliminate asymptotic time dependence at $T \gg T_0$ for a uniform medium. The solid thick line is for $\nu \approx \nu_c(T_0)$, the {dashed thick line} is for $\nu \approx \nu_{c,10 \text{ per cent}}(T_0)$, and the {dotted thick line} is for $\nu \approx \nu_{c,90 \text{ percent}}(T_0)$. The remaining curves are spaced by a factor of ≈ 15 in frequency in the top panel and by a factor of ≈ 8 in the middle and bottom panels.
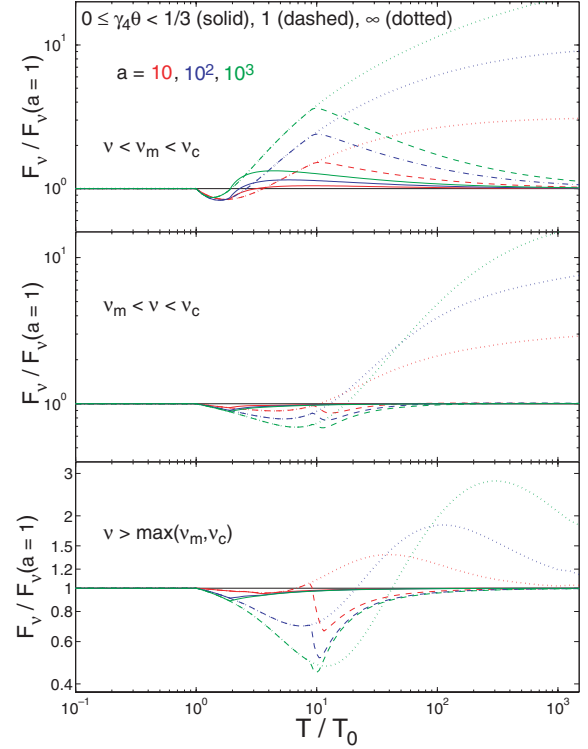

Figure 13. The ratio of the flux with and without a density jump at $R > R_0$, within a finite angle $\theta < \theta_{\max}$ around the line of sight, for three different density contrasts ($a = 10, 100$ and 1000) and three different angular sizes ($\gamma_4\theta_{\max} = 1/3, 1$ and ∞). This serves as an approximate upper limit for the effect of a clump in the external medium on the light curve. The different panels are for the most relevant PLSs of the synchrotron spectrum.

Fig. 13 shows the results of this model for a density clump that lies along the line of sight, $\theta_{\min} = 0$ and $\gamma_4\theta_{\max} = 1/3, 1, \infty$ while $\Delta\phi = 2\pi$, for three different values of the density contrast ($a = 10, 100, 1000$) and for the three most relevant PLSs of the spectrum (that were modelled in Section 3.2). The smaller the angular extent of the clump, the smaller the amplitude of the change in the flux *relative* to its value for the smooth underlying density distribution without the clump ($a = 1$), and the smaller the factor in time over which it effects the flux significantly (e.g. the full width at half-maximum of the *relative* flux). This behaviour is expected since both the amplitude and the duration of the fluctuation depend on the size of the clump (Ioka et al. 2005). The amplitude depends on the ratio in size between the perturbed region (of length-scale l_{cl}) and the unperturbed region (of length-scale R/γ) of the blast wave, and thus increases with l_{cl}. The duration depends on the delay in the arrival time of photons emitted from the perturbed region, which again increases with the size of this region.

As can be seen in Fig. 13, the amplitude of the fluctuation in the relative flux increases with the density contrast a. There is a sharp transition in the light curve at $\tilde{T} = 1 + 2(4 - k_0)(\gamma_4\theta_{\max})^2$, when the radiation from the outer edge of the clump at $R = R_0$ reaches the observer, which corresponds to the peak in the relative flux for $\gamma_3\theta_{\max} = \gamma_4\theta_{\max} \psi^{-1} \sim 1$. Such sharp features (see also Fig. 14) are caused by the oversimplified clump model that we use here, and are expected to be smoothed out in more realistic models of clumps. Above ν_m a clump can produce a dip or a bump in the relative flux

with a relatively small amplitude (depending on its size and density contrast), while below ν_m it produces a bump in the relative flux with a larger amplitude.

Fig. 14 shows the *relative* flux for a fixed density contrast, $a = 100$, for three clumps along the line of sight with different angular sizes ($\Delta\phi = 2\pi$, $\theta_{\min} = 0$ and $\gamma_4\theta_{\max} = 0.1, 1/3, 1$), as well as for a clump close to the edge of the visible region at the time of the collision, $\gamma_4(\theta_{\min}, \theta_{\max}) = (2/3, 4/3)$ and $\Delta\phi = \pi/6$, which occupies the same solid angle as the clump along the line of sight with $\gamma_4\theta_{\max} = 1/3$. The effect of a given clump on the light curve is maximal when it is along the line of sight, and it becomes smaller the further it is from the line of sight (i.e. its effect is significant over a shorter time-scale and the amplitude of the change in the relative flux is somewhat reduced).

Overall, a fairly large clump of size $l_{cl} \gtrsim R/\gamma$ with a sufficiently large density contrast ($a \gtrsim 10 - 10^2$) is required in order to produce an observable signature in the light curve, and even then the most prominent signal would be below ν_m, which is typically relevant for the radio. In the optical, which is typically above ν_m, there would only be a small dip or bump in the relative flux, which would be hard to detect.

6 IMPLICATIONS TO GRBS 021004, 000301C, 030329 AND SHB 060313

Next we reconsider the cause for the fluctuations in the optical afterglow light curves of the long-soft GRBs 021004, 000301C and 030329 as well as the very recent short-hard GRB 060313, in light of
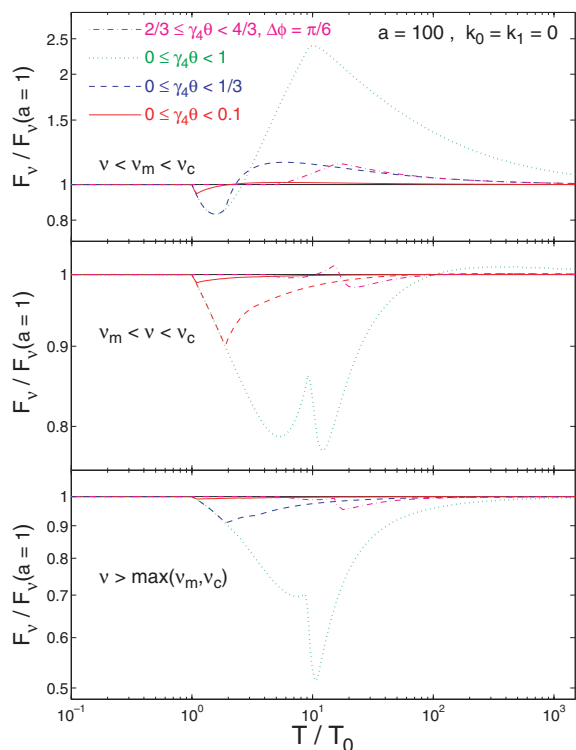
Figure 14. Same as Fig. 13 but for a fixed density contrast, $a = 100$, and for three clumps along the line of sight together with a clump that is at the side of the visible region at the time of collision, centred around $\gamma_4\theta \approx 1$.

our results. In all these bursts, there are rebrightening episodes that follow a rather smooth power-law decay and therefore our results can be used in order to test whether these rebrightenings can be a result of a self-similar blast wave that encounter a density clump.

GRB 021004 showed significant variability in its optical afterglow (Pandey et al. 2002; Bersier et al. 2003; Fox et al. 2003; Uemura et al. 2003) which included three clear distinct episodes of mild rebrightening ($\alpha \gtrsim 0$) at $T \sim 0.05$, ~ 0.8 and ~ 2.6 d. Just before the first of these epochs, the decay seems to be a smooth power law with $\alpha \sim -0.7$, although the observations are sparse and earlier variability may be present. At $T \sim 0.05$ d α becomes positive over a factor of ~ 2–3 in time. Assuming that indeed the early decay is a power law such a large increase in α over a relatively small factor in time is hard to accommodate by a jump in the external density: $\Delta\alpha \sim 1$ requires $a \gtrsim 10^2$ and even then it is hard to achieve such an increase in α over a factor of ~ 2–3 in time. The second rebrightening episode lies within the tail of the first, and is therefore not a very 'clean' case to study. The third rebrightening epoch at ~ 2.6 d is somewhat more isolated, and has $\Delta\alpha \gtrsim 1$ where most of the increase in α is within about a factor of ~ 1.5 in time. This is extremely hard to achieve by variations in the external density. On the other hand, angular fluctuations in the energy per solid angle within the jet (a 'patchy shell') (Granot & Königl 2003; Nakar & Oren 2004) or multiple episodes of energy injection (Björnsson, Gudmundsson & Jóhannesson 2004; de Ugarte Postigo et al. 2005), suggested to account for both the fluctuations in the light curve and the variability in the linear polarization of this afterglow .

GRB 000301C displayed a rough power-law decay that is followed by a largely achromatic bump in its optical to NIR light curves (Sagar et al. 2000; Berger et al. 2000) peaking at $T \sim 3.8$ d. Before the bump $\alpha \approx -(1.2$–1.3$)$ and during the rise to the bump

α became slightly positive, so that $\Delta\alpha \sim 1.5$, where most of the increase in α occurred over a factor of ~ 1.5 in time. Our results strongly suggest that this cannot be produced by a sudden change in the external density (as has been suggested by Berger et al. 2000). The decay just after the peak of the bump is very sharp, $\alpha \approx -(3.5 - 4)$, and since $\beta - \alpha > 2$ (Sagar et al. 2000 find $\beta = -0.96 \pm 0.08$ during the decay just after the peak at $T = 4.8$ d) this requires a deviation from spherical symmetry (Kumar & Panaitescu 2000). In this case an alternative microlensing interpretation (Garnavich et al. 2000) was shown to be able to reproduce the shape of the bump (Gaudi et al. 2001).

GRB 030329 has one of the best monitored and densely sampled optical afterglow light curves to date. It is presented in great detail by Lipkin et al. (2004) who clearly show that the light curve contains several rebrightening ($\alpha > 0$) episodes in which $\Delta\alpha > 2$. All of these episodes have a similar structure where a smooth power-law decay is followed by a very sharp ($\Delta T < T$) rebrightening. Pe' er & Wijers (2006) have suggested that the first (and largest) rebrightening episode is the signature of a wind termination shock. Our results which show that such a wind termination shock produces a much smoother light curve (Section 4.1) strongly disfavor this explanation. Sheth et al. (2003) have followed Berger et al. (2003) in attributing the first rebrightening episode to a two-component jet, but argued that the subsequent rebrightening episodes could be explained by variations in the external density in a roughly quasi-spherical configuration (set by the wide jet). Our results suggest that these bumps in the optical light curve of GRB 030329 cannot be a result of density bumps, implying that the two-component jet model of Berger et al. (2003) and Sheth et al. (2003) fails to account for most of the observed light curve fluctuations.

Finally, the optical light curve of GRB 030329 shows a break in the power-law decay at $T_{break} \approx 0.5$ d, suggesting a jet break. Our results do not address directly a blast wave that encounters a density jump after its Lorentz factor falls below the inverse of its half-opening angle. In order to constrain this case, we consider a jet that is not spreading sideways and thus behaves hydrodynamically as a wedge taken out of a spherical solution (as discussed in Section 2). Using our semi-analytical model, we calculate the light curves for $a = 2$, 10 and 100 taking $T_0 \approx 3T_{break}$. Significant rebrightening was not observed in any of these cases. This result is not surprising since the line of sight optical emissivity actually slightly *drops* for a density jump, and in the case of a post-jet-break there is no large angle emission to compensate for this drop. Similar result was obtained by Huang, Cheng & Gao (2006) that explored the case of GRB 030329 assuming that the jet spreads sideways. Thus we find that density variations are very unlikely to be the source of the variability observed in this afterglow. An alternative variability source that might be able to account for the short observed time-scales is a late-time energy injection by 'refreshed shocks' (Granot et al. 2003; Huang et al. 2006).

The afterglow of the very recent short-hard GRB 060313 has been monitored both by the X-ray Telescope (XRT) and by the optical/Ultraviolet Telescope (UVOT) onboard *Swift* (Roming et al. 2006). The optical/UV light curve showed three sharp bumps/flares at $T \sim 1.7$, ~ 3.2 and ~ 6.6 h, with an amplitude of more than a factor of 2 in flux and a very short rise time of $\Delta T \lesssim 0.1T$. During the same time, the X-ray light curve showed a smooth (and steeper) power-law decay. This was interpreted by Roming et al. (2006) as the result of variations in the external density by a factor of ~ 2, where the lack of variability in the X-rays was attributed to ν_c being between the optical/UV and the X-rays. Our results show that such sharp rebrightening episodes as were seen in the

optical/UV afterglow light curve of GRB 060313, especially with no indication in the X-rays, are not expected from variations in the external density. Therefore, other cause for this variability is much more likely, such as late-time internal shocks with a very soft spectrum, as was suggested by Roming et al. (2006) as an alternative mechanism.

7 CONCLUSIONS

We have presented a semi-analytic model for the light curve resulting from synchrotron emission by a spherical relativistic adiabatic blast wave that propagates into a power-law external density profile with a single sharp density jump at some radius R_0. Our solution is general enough to include a transition in the density power-law index (k) at R_0, but is limited to cases in which the blast wave is self-similar before and remains relativistic after it encounters the density jump. This model has been used to explore in detail two density profiles that are most relevant to GRB afterglows: a wind termination shock, and a sharp density jump between two regions of uniform density. The latter results are also used to constrain the signature of density clumps in a uniform medium. We have also carried out detailed numerical simulations for several of the cases which we have studied in detail. These numerical results serve three purposes. First, they are used in order to obtain more accurate light curves for the cases which are of special interest. Secondly, they are appropriate for calculating the light curves in the vicinity of a spectral break frequency (Section 4.3). Thirdly, they serve as a test for the quality of our simple semi-analytic model, which is found to give a very good qualitative description and reasonable quantitative description of the light curve.

Our main result is that within the scenario considered in this work density jumps do not produce sharp features in the light curve, regardless of their density contrast (see Section 2 for a discussion of the limitations and applicability of our results). The results of our specific case studies are as follows.

(i) *A wind termination shock.*

(1) The light curve shows a smooth transition, which lasts for about one decade in time, between the asymptotic power-law behaviour at $T < T_0$ and at $T \gg T_0$.

(2) There is no rebrightening or any other sharp feature that can be used as a clear observational signature.

(3) Above the cooling frequency, ν_c, there is no change in the asymptotic value of the temporal index, α, and it only fluctuates with a small amplitude ($\Delta\alpha \approx 0.1$).

(4) The only observable signatures of a wind termination shock are a smooth break, with an increase of $\Delta\alpha = 0.5$ in α, below ν_c and a transition in the temporal evolution of ν_c.

(ii) *A density jump between two uniform density regions.*

(1) The light curve shows a smooth transition between the two asymptotic power laws (at $T < T_0$ and $T \gg T_0$).

(2) The transition time increases with the density contrast, a, and is about $\sim 10aT_0$.

(3) The maximal deviation, $\Delta\alpha_{max}$, of the temporal index α from its asymptotic value (at $T < T_0$ and $T \gg T_0$) is small. For example, $\Delta\alpha_{max}(a = 10) < 0.4$; $\Delta\alpha_{max}$ depends weakly on a and approaches ≈ 1 at very large a values. Therefore, a density jump cannot produce an optical rebrightening when $\nu_{optical} > \nu_m$.

(4) The light curve fluctuates also above ν_c (typically including the X-ray band). While the asymptotic flux (at $T \gg T_0$) above ν_c is unaffected by the density jump, the fluctuations in α are *comparable* to those below ν_c.

(iii) *An overdense clump on top of a uniform density background.*

(1) Only a fairly large clump ($l_{cl} \gtrsim R/\gamma$) with a sufficiently large density contrast ($a \gtrsim 10 - 10^2$) produces a significant fluctuation in the light curve.

(2) The effect of a clump on the light curve is significantly larger when it is located along the line of sight than at an angle of $\sim 1/\gamma$ from the line of sight.

(3) The signature of a clump is most apparent at $\nu < \nu_m < \nu_c$.

(4) Above ν_m a clump can actually cause a small dip in the light curve, while below ν_m it causes a (larger) bump.

For a spherical density jump, our conclusions are based on accurate results, while in the case of a density clump we obtain only an approximate upper limit for its effect on the light curve. Therefore, our results for density clumps should be taken only as rough guidelines. Our main results remain valid also when the observed frequency is close to a spectral break frequency around the time of the density jump.

Our conclusions are different from those of previous works that explored similar physical configuration. Previous works predicted a significant optical rebrightening, and rather sharp features in the afterglow light curve. The main cause for this difference is our consideration of both the effect of the reverse shock on the dynamics (which we find cannot be neglected even when $a \sim 2$) and the arrival time of the photons to the observer from different parts of the emitting regions. Both of these effects tend to smoothen the light curve significantly.

Finally, we considered the implications of our results for the origin of the fluctuations in the highly variable light curves of four GRBs (three long-soft GRBs and one short-hard GRB). We find that if these afterglows are produced by external shocks then density variations are unlikely to be the source of the fluctuations in any of these bursts.

REFERENCES

Baltz E. A., Hui L., 2005, ApJ, 618, 403
Berger E. et al., 2000, ApJ, 545, 56
Berger E. et al., 2003, Nat, 426, 154
Bersier D. et al., 2003, ApJ, 584, L43
Björnsson G., Hjorth J., Pedersen K., Fynbo J. U., 2002, ApJ, 579, L59
Björnsson G., Gudmundsson E. H., Jóhannesson G., 2004, ApJ, 615, L77
Blandford R. D., McKee C. F., 1976, Phys. Fluids, 19, 1130 (BM)
Burrows D. N. et al., 2005, Sci, 309, 1833
Cannizzo J. K., Gehrels N., Vishniac E. T., 2004, ApJ, 601, 380
Chevalier R. A., Li Z.-Y., 2000, ApJ, 536, 195
Covino S., Ghisellini G., Lazzati D., Malesani D., 2003, in Piro L., Feroci M., eds, ASP Conf. Ser. Vol. 312, Gamma-Ray Bursts in the Afterglow Era Third Rome Workshop on. Astron. Soc. Pac., San Francisco, p. 169
Dai Z. G., Lu T., 2002, ApJ, 565, L87
Dai Z. G., Wu X. F., 2003, ApJ, 591, L21
Dermer C. D., 2007a, ApJ, 664, 384
Dermer C. D., 2007b, preprint (astro-ph/0703223)
Dermer C. D., Mitman K. E., 1999, ApJ, 513, L5
de Ugarte Postigo A. et al., 2005, A&A, 443, 841

Eldridge J. J., Genet F., Daigne F., Mochkovitch R., 2006, MNRAS, 367, 186
Falcone A. D. et al. (the Swift Xrt Team), 2006, in Holt S. S., Gehrels N., Nousek J. A., eds, AIP Conf. Proc. Vol. 836, Gamma Ray Bursts in the Swift Era: Sixteenth Maryland Astrophysics Conference. Am. Inst. Phys., New York, p. 386
Fox D. W. et al., 2003, Nat, 422, 284
Fryer C. L., Rockefeller G., Young P. A., 2006, ApJ, 647, 1269
Garnavich P. M., Loeb A., Stanek K. Z., 2000, ApJ, 544, L11
Gaudi B. S., Granot J., Loeb A., 2001, ApJ, 561, 178
Gorosabel J. et al., 2006, ApJ, 641, L13
Granot J., Königl A., 2003, ApJ, 594, L83
Granot J., Sari R., 2002, ApJ, 568, 820
Granot J., Miller M., Piran T., Suen W. M., Hughes P. A., 2001, in Costa E., Frontera F., Hjorth J., eds, Gamma-ray Bursts in the Afterglow Era. Springer, Berlin, p. 312
Granot J., Nakar E., Piran T., 2003, Nat, 426, 138
Harrison F. A. et al., 2001, ApJ, 559, 123
Heyl J. S., Perna R., 2003, ApJ, 586, L13
Huang Y.-F., Tan C.-Y., Dai Z.-G., Lu T., 2002, Chinese Astron. Astrophys., 26, 414
Huang Y. F., Cheng K. S., Gao T. T., 2006, ApJ, 637, 873
Ioka K., Kobayashi S., Zhang B., 2005, ApJ, 631, 429
Kobayashi S., Sari R., 2000, ApJ, 542, 819
Kobayashi S., Piran T., Sari R., 1999, ApJ, 513, 669
Krimm H. A. et al., 2007, ApJ, in press (astro-ph/0702603)
Kumar P., Panaitescu A., 2000, ApJ, 541, L51
Kumar P., Piran T., 2000a, ApJ, 532, 286
Kumar P., Piran T., 2000b, ApJ, 535, 152
Laursen L. T., Stanek K. Z., 2003, ApJ, 597, L107
Lazzati D., Rossi E., Covino S., Ghisellini G., Malesani D., 2002, A&A, 396, L5
Lipkin Y. M. et al., 2004, ApJ, 606, 381
Masetti N. et al., 2000, A&A, 359, L23
Matheson T. et al., 2003, ApJ, 599, 394
Meszaros P., 2006, Rep. Prog. Phys., 69, 2259
Nakar E., 2007, Phys. Rep., 442, 166
Nakar E., Oren Y., 2004, ApJ, 602, L97
Nakar E., Piran T., 2003, ApJ, 598, 400
Nakar E., Piran T., 2004, MNRAS, 353, 647
Nakar E., Piran T., Granot J., 2003, New Astron., 8, 495
Nousek J. A., Kouveliotou C., Grupe D., Page K., Granot J., Ramirez-Ruiz E. et al., 2006, ApJ, in press (astro-ph/0508332)
O'Brien P. T. et al., 2006, ApJ, 647, 1213
Panaitescu A., 2005, MNRAS, 363, 1409
Panaitescu A., 2007, MNRAS, 379, 331
Panaitescu A., Kumar P., 2000, ApJ, 543, 66
Pandey S. B. et al., 2002, Bull. Astron. Soc. India, 31, 19
Pe' er A., Wijers R. A. M. J., 2006, ApJ, 643, 1036
Piran T., 2005, Rev. Mod. Phys., 76, 1143
Ramirez-Ruiz E., Merloni A., Rees M. J., 2001a, MNRAS, 324, 1147
Ramirez-Ruiz E., Dray L. M., Madau P., Tout C. A., 2001b, MNRAS, 327, 829
Ramirez-Ruiz E., García-Segura G., Salmonson J. D., Pérez-Rendón B., 2005, ApJ, 631, 435
Rees M. J., Mészáros P., 1998, ApJ, 496, L1
Rhoads J. E., 1997, ApJ, 487, L1
Rhoads J., 1999, ApJ, 525, 737
Roming P. W. A. et al., 2006, ApJ, 651, 985
Rybicki G. B., Lightman A. P., 1986, in George B. Rybicki, Alan P., eds, Lightman Radiative Processes in Astrophysics. Wiley-VCH, New York, p. 400
Sagar R., Mohan V., Pandey S. B., Pandey A. K., Stalin C. S., Castro Tirado A. J., 2000, Bull. Astron. Soc. India, 28, 499
Sari R., Esin A. A., 2001, ApJ, 548, 787
Sari R., Mészáros P., 2000, ApJ, 535, L33
Sari R., Piran T., 1995, ApJ, 455, L143
Sari R., Piran T., Halpern J., 1999, ApJ, 519, L17

Sato R., Kawai N., Suzuki M., Yatsu Y., Kataoka J., Takagi R., Yanagisawa K., Yamaoka H., 2003, ApJ, 599, L9
Sheth K., Frail D. A., White S., Das M., Bertoldi F., Walter F., Kulkarni S. R., Berger E., 2003, ApJ, 595, L33
Stanek K. Z., Garnavich P. M., Kaluzny J., Pych W., Thompson I., 1999, ApJ, 522, L39
Stanek K. Z. et al., 2007, ApJ, 654, L21
Tam P. H., Pun C. S. J., Huang Y. F., Cheng K. S., 2005, New Astron., 10, 535
Uemura M., Kato T., Ishioka R., Yamaoka H., 2003, PASJ, 55, L31
Uemura M. et al., 2004, PASJ, 56, S77
Wang X., Loeb A., 2000, ApJ, 535, 788
Wei D. M., Lu T., 1998, ApJ, 505, 252
Wijers R. A. M. J., 2001, in Costa E., Frontera F., Hjorth J., eds, Gamma Ray Bursts in the Afterglow Era. Springer, Berlin, p. 306
Wijers R. A. M. J., Rees M. J., Meszaros P., 1997, MNRAS, 288, L51
Zhang B., Fan Y. Z., Dyks J., Kobayashi S., Mészáros P., Burrows D. N., Nouesk J. A., Gehrels N., 2006, ApJ, 642, 354

APPENDIX A: A ONE-DIMENSIONAL SPECIAL RELATIVISTIC HYDRODYNAMICS AND RADIATION CODE

In order to obtain accurate light curves while relying on a minimal number of approximations, we use a one-dimensional special relativistic hydrodynamic code and combine it with an optically thin synchrotron radiation module. This is the same code that was used before in Nakar & Piran (2004). We use a one-dimensional hydrodynamic code that was generously provided to us by Re' em Sari and Shiho Kobayashi. It is a Lagrangian code based on a second-order Gudanov method with an exact ultra-relativistic Riemann solver and it is described and used in Kobayashi, Piran & Sari (1999) and Kobayashi & Sari (2000). On top of this code we have constructed a module that calculates the resulting optically thin synchrotron radiation. The code does not include the synchrotron self-absorption or synchrotron self-Compton processes. The effect of the radiation on the hydrodynamics is neglected. Below we describe the physics that is included in the radiation module.

Having the full hydrodynamic evolution of the fluid (from the hydrodynamic code), we first identify the time-steps in which a given fluid element is shocked by finding episodes of increase in its entropy. The same fluid element can be shocked many times. Once a fluid element is shocked, all its electrons are assumed to be instantly accelerated into a power-law energy distribution with an index p, $dN/d\gamma_e \propto \gamma_e^{-p}$ for $\gamma_e > \gamma_{min}$. The energy in the electrons is taken as a constant fraction, ϵ_e, of the internal energy, and this condition determines γ_{min} (it is assumed that $p > 2$). From this point onwards, and until the same fluid element is shocked again, the electron energy distribution decouples from the internal energy and evolves through radiative cooling and adiabatic cooling or heating (pdV work). The magnetic energy in each fluid element is taken to be a constant fraction, ϵ_B, of the internal energy at all times.

One of the main difficulties in calculating the synchrotron radiation at high frequencies is the short cooling time, which may be much shorter than the hydrodynamic time-steps. Additionally, exact (numerical) integration of the emission while keeping track of the exact form of the evolved electron distribution would significantly increase the code running time. In order to overcome these difficulties, we calculate the radiation during any hydrodynamic time-step using an analytic approximation, in the following way. Immediately after a fluid element crosses a shock, its initial electron energy distribution is taken to be a power law (with index p) between γ_{min} and $\gamma_{max} = \infty$. From this point onwards, we calculate the evolution

of γ_{min} and γ_{max} with time. Their values at the end of a time-step are taken as the initial values for the next time-step in which the initial distribution of the electron Lorentz factors is taken, again, as a power law between the new values of γ_{min} and γ_{max}. From the point where γ_{max} becomes comparable to γ_{min} (within a factor of 2), namely when there is fast cooling (i.e. when all of the electrons in the given fluid element have cooled significantly due to radiative losses, after having been accelerated at the shock crossing), the electron energy distribution is taken as a delta function.

The evolution of γ_{min} and γ_{max} is dictated by radiative and adiabatic losses (or gains):

$$\frac{d\gamma_e}{dt'} = -c_r\gamma_e^2 + c_a\gamma_e. \tag{A1}$$

Here $c_r = \sigma_T(B')^2/(6\pi\, m_e\, c) > 0$ is the radiative cooling coefficient, where B' and t' are the magnetic field and time, respectively, measured in the comoving frame of the emitting fluid element, σ_T is the Thomson cross-section, m_e is the electron rest mass, and $c_a = (1/3)(d \ln n'/dt')$ is the adiabatic cooling/heating coefficient where n' is the fluid proper number density for an adiabatic index of 4/3 (more generally, for an adiabatic index of $\hat{\gamma}$, the factor of 1/3 is replaced by $\hat{\gamma} - 1$). Note that c_r is negative when the fluid element expands (adiabatic cooling) and positive when it is compressed (adiabatic heating). The coefficients c_r and c_a are taken to be constants within each hydrodynamical time-step, and $\gamma_e(t', \gamma_{e,0})$ is found by integrating over equation (A1), where t' is the time since the beginning of the time-step and $\gamma_{e,0} = \gamma_e(t' = 0)$:

$$\gamma_e(t', \gamma_{e,0}) = \left\{ \frac{1}{\gamma_{e,0}} \exp\left(-c_a t'\right) + \frac{c_r}{c_a}\left[1 - \exp\left(-c_a t'\right)\right] \right\}^{-1}. \tag{A2}$$

Given the evolution of γ_{max} and γ_{min} with time, we can find radiation critical times within a given hydrodynamical time-step. A good example is the time when γ_{max} or γ_{min} drops below the value that corresponds to a synchrotron frequency equal to the observed frequency, $\gamma_{e,\nu}$, where $\nu_{syn}(\gamma_{e,\nu}) \equiv \nu_{obs}$ (thereby solving the problem of short cooling time-scales at very high frequencies).

Thus, any hydrodynamical time-step is divided into shorter radiation time-steps. The (time-averaged) rest-frame emissivity density (radiated energy per unit volume, time and frequency) at frequency ν' during a radiation time-step with a duration t'_f is

$$P'_{\nu'} = \frac{1}{t'_f} \int_0^{t'_f} dt' \int_{\gamma_{min}(t)}^{\gamma_{max}} d\gamma_e\, \frac{dn'(\gamma_e)}{d\gamma_e}\, P'_{e,\nu'}(\gamma_e), \tag{A3}$$

where $P'_{e,\nu'}(\gamma_e)$ is the emitted power per unit frequency per electron, and $[d\, n'(\gamma_e)/d\,\gamma_e]\, d\,\gamma_e$ is the proper number density of electrons with Lorentz factors between γ_e and $\gamma_e + d\,\gamma_e$. In order to derive analytic solutions to equation (A3), we further approximated $\gamma_{min}(t')$ and $\gamma_{max}(t')$. In cases where $d\,\gamma_e/d\, t' < 0$, we use the radiative cooling curve (the solution of equation A1 for $c_a = 0$):

$$\gamma_r(t', \gamma_{e,0}) = \left(\frac{1}{\gamma_{e,0}} + \frac{t}{\tau} \right)^{-1}, \tag{A4}$$

adjusting τ so that $\gamma_r(t'_f) = \gamma_e(t'_f, \gamma_{e,0})$ where the latter is evaluated using equation (A2) with the true value of c_a (for $c_a = 0$ the cooling time-scale τ is equal to $1/c_r$). In cases where $d\,\gamma_e/d\, t' > 0$ (rare cases where the adiabatic heating dominates radiative cooling), we use linear heating with time such that $\gamma_e(t'_f, \gamma_{e,0})$ is given by equation (A2). Using these two cases for $\gamma_e(t', \gamma_{e,0})$, we integrate analytically over equation (A3) while approximating the electron distribution as a power law between $\gamma_{min}(t')$ and $\gamma_{max}(t')$ (or as a delta function if $\gamma_{max}/\gamma_{min} < 2$).

Since we use a one-dimensional hydrodynamical code in spherical coordinates, which explicitly assumes spherical symmetry, each fluid element represents a thin spherical shell. Once the rest-frame spectral power of a fluid element is calculated, we integrate over the contribution of this shell to the observed flux at a given observer time and observer frequency. This calculation takes into account the appropriate Lorentz transformation of the radiation field and photon arrival time from each point along the shell.

This paper has been typeset from a TEX/LATEX file prepared by the author.